J. Mech. Phys. Solids 192 (2024) 105787

Contents lists available at ScienceDirect

Journal of the Mechanics and Physics of Solids

journal homepage: www.elsevier.com/locate/jmps

Unstructured growth of irregular architectures for optimized metastructures

Yingqi Jia [a], Ke Liu [b], Xiaojia Shelly Zhang [a,c,d,*]

[a] Department of Civil and Environmental Engineering, University of Illinois Urbana-Champaign, Urbana, IL 61801, USA
[b] Department of Advanced Manufacturing and Robotics, Peking University, Beijing 100871, China
[c] Department of Mechanical Science and Engineering, University of Illinois Urbana-Champaign, Urbana, IL 61801, USA
[d] National Center for Supercomputing Applications, Urbana, IL 61801, USA

ARTICLE INFO

Keywords:
Topology optimization
Unstructured growth
Transformation
Virtual growth
Metastructure

ABSTRACT

Mechanical metastructures have been prevailing recently owing to their unusual mechanical responses. Despite notable progress in designing periodic metastructures, creating irregular and stochastic metastructures with optimized performance remains challenging because of the enlarged design space. In this study, we introduce a novel approach to realize the unstructured growth of irregular architectures for optimized metastructures. A "growth"-like design scheme is proposed to facilitate random yet controllable growth of predefined building blocks on an unstructured graph toward desired bulk properties. We also formulate a topology optimization framework that simultaneously optimizes building block selection and transformation (scaling, skew, and rotation) to generate metastructures with various optimized mechanical functionalities. These functionalities are achieved by harnessing the diverse homogenized material properties spanned by various frequency combinations of building blocks and the microstructure's transformations. We discover metastructures that ensure geometric integrity and exhibit explicitly controllable and globally uniform feature sizes beneficial for fabrication. Moreover, the transformation-based topology optimization ensures these metastructures naturally conform to the boundaries of the design domain and can serve as mechanical infills. The proposed approach holds promise for uncovering optimized metastructures applicable across a wide array of engineering applications.

1. Introduction

Metamaterials and metastructures have become increasingly popular thanks to their advantageous material properties and structural responses. In the field of mechanical metamaterials and metastructures, great advances have been made in achieving various functionalities, such as enhanced failure resistance (Zhang et al., 2018b; Cai et al., 2021; Deng et al., 2023; Chen et al., 2024; Jia et al., 2023), negative Poisson's ratio (Clausen et al., 2015), negative mass density (Chen et al., 2017), energy dissipation (Ni and Gao, 2019), impact mitigation (Ou et al., 2024), custom stress–strain/force–displacement responses (Zhang et al., 2018a; Li et al., 2023), to name a few.

Significant advances have been made in mechanical metamaterials and metastructures, and most studies have focused on periodic or nearly periodic designs. These designs typically involve the periodic tiling of motifs with parameterized geometries. However, upon closer examination of natural materials (Rho et al., 1998; Barthelat et al., 2006; Hosoya et al., 2007), many of them exhibit

* Corresponding author at: Department of Civil and Environmental Engineering, University of Illinois Urbana-Champaign, Urbana, IL 61801, USA.
E-mail address: zhangxs@illinois.edu (X.S. Zhang).

https://doi.org/10.1016/j.jmps.2024.105787
Received 6 May 2024; Received in revised form 12 July 2024; Accepted 12 July 2024
Available online 17 July 2024

irregular (aperiodic) and stochastic patterns. These patterns have demonstrated a wide array of practical functionalities, including body protection (Rhee et al., 2009) and flight agility (Sharma and Hiremath, 2022). Thus, we focus on irregular architectures in this work.

Recent studies have started to explore irregular metamaterials and metastructures by effectively parameterizing the design space using various techniques. These techniques include filtered random lattice (Reid et al., 2018; Mirzaali et al., 2019; Portela et al., 2020), phase-separation induced spinodal foam (Kumar et al., 2020; Zheng et al., 2021; Senhora et al., 2022), and bio-inspired virtual growth (Jia et al., 2024a,b). Among these approaches, the virtual growth-based ones (Jia et al., 2024a,b) optimize the frequency combination of building blocks and subsequently grow them to form the metastructure using the virtual growth algorithm extended upon Liu et al. (2022). The resulting metastructures are seamlessly integrated and exhibit a uniform feature size that facilitates fabrication.

While virtual growth-based approaches (Jia et al., 2024a,b) have shown initial success in creating metastructures with diverse functionalities, they focus on growing building blocks on a structured graph — more precisely, a mesh with square elements in two dimensions (2D) and cubic elements in three dimensions (3D). Consequently, the building blocks are arranged in horizontal and vertical directions. However, it is widely recognized that optimal structural members should align with the principal directions of the structural response field, such as the stress field, which is often complex and spatially varying, rather than strictly horizontal and vertical. Therefore, introducing transformations (scaling, skew, and/or rotation) to the optimized building blocks could further enhance design performance. The performance gain brought by building block transformation has been commonly leveraged (Wu et al., 2021), for example, by directly optimizing building block transformation (Zhu et al., 2019; Li et al., 2022) or identifying target transformations through de-homogenization approaches (Stutz et al., 2020; Groen et al., 2021; Wang et al., 2022b; Jensen et al., 2024).

In the present study, we introduce a novel methodology (Fig. 1) aimed at discovering metastructures with target mechanical responses through simultaneous optimization of building block selection and the microstructure's transformation. To establish this methodology, we develop an unstructured virtual growth algorithm designed to grow transformed metastructures. As shown in Fig. 1(a), we begin with simple but representative building blocks and aim to seamlessly grow them into a given unstructured mesh to achieve the target frequency combination. After filling the building blocks one by one, we generate a transformed metastructure exhibiting the desired building block distribution and transformation. This unstructured virtual growth can create complex patterns in both 2D and 3D and forms the foundation of the proposed methodology.

In addition to the unstructured virtual growth algorithm, we also investigate the constitutive relationship between microstructural transformation and homogenized elasticity (Fig. 1(b)). Unlike many existing studies that rely on conformal mapping, our approach incorporates all three types of transformations — relative scaling ($\overline{\chi}$), skew ($\overline{\theta}$), and rotation ($\overline{\varphi}$) — to enlarge the achievable homogenized material properties as demonstrated by the diverse elasticity surfaces.

Once obtaining the constitutive relationship between microstructural transformation and homogenized elasticity, we introduce frequency- and transformation-based topology optimization to generate optimized metastructures with various functionalities. As shown in Fig. 1(c), given a design domain subjected to applied traction ($\overline{t}$) and displacement ($\overline{u}$) loadings, we optimize the presence of microstructures at each location. If a microstructure exists, we further optimize the frequency combination of building blocks that form the microstructure as well as the microstructure's transformation. By simultaneously optimizing these three variable types, we aim to achieve diverse mechanical functionalities, including stiffness maximization, unidirectional mechanical cloaking, and local stiffness control. Guided by optimized variables, we leverage unstructured virtual growth (Fig. 1(a)) to discover metastructures with various optimized functionalities (Fig. 1(c)). In addition to attaining target mechanical responses, the optimized metastructures inherit a uniform feature size from the selected building blocks, which is crucial for manufacturing. Moreover, the optimized metastructure naturally conforms to the boundaries of the design domain without the need for post-processing, therefore enabling the design to seamlessly function as mechanical infills.

The remaining parts of the paper are organized as follows. We begin in Section 2 by introducing the proposed unstructured virtual growth algorithm. Next, in Section 3, we derive the constitutive relationship between the homogenized elasticity matrix and the frequency combination of building blocks as well as microstructural transformation. In Section 4, we present a topology optimization framework for discovering transformed metastructures with optimized mechanical performance, where we also elucidate the transformation-guided mesh generation used for growing building blocks. Subsequently, we provide three numerical examples in Section 5 to illustrate the discovered metastructures and the underlying mechanisms for optimized mechanical responses. Finally, several concluding remarks are drawn in Section 6.

Six appendices further complement this paper. Appendix A introduces the adjacency rules used in the unstructured virtual growth algorithm. Appendix B recaps the numerical homogenization theory in Vigliotti and Pasini (2012), which is utilized to predict the homogenized elasticity matrix in this work. Appendix C derives the global stiffness matrix of microstructures under uniform scaling. Appendix D briefly introduces the homogenized elasticity matrix of microstructures after rotation. Appendix E presents the sensitivity analysis and verification employed in topology optimization, and finally Appendix F compares the optimized periodic and aperiodic metastructures for stiffness maximization.

2. Unstructured virtual growth algorithm

As discussed earlier, the unstructured virtual growth algorithm enables the growing of the microstructure towards optimized bulk properties. In this section, we propose the unstructured virtual growth algorithm. We also briefly review the classical (Liu et al.,

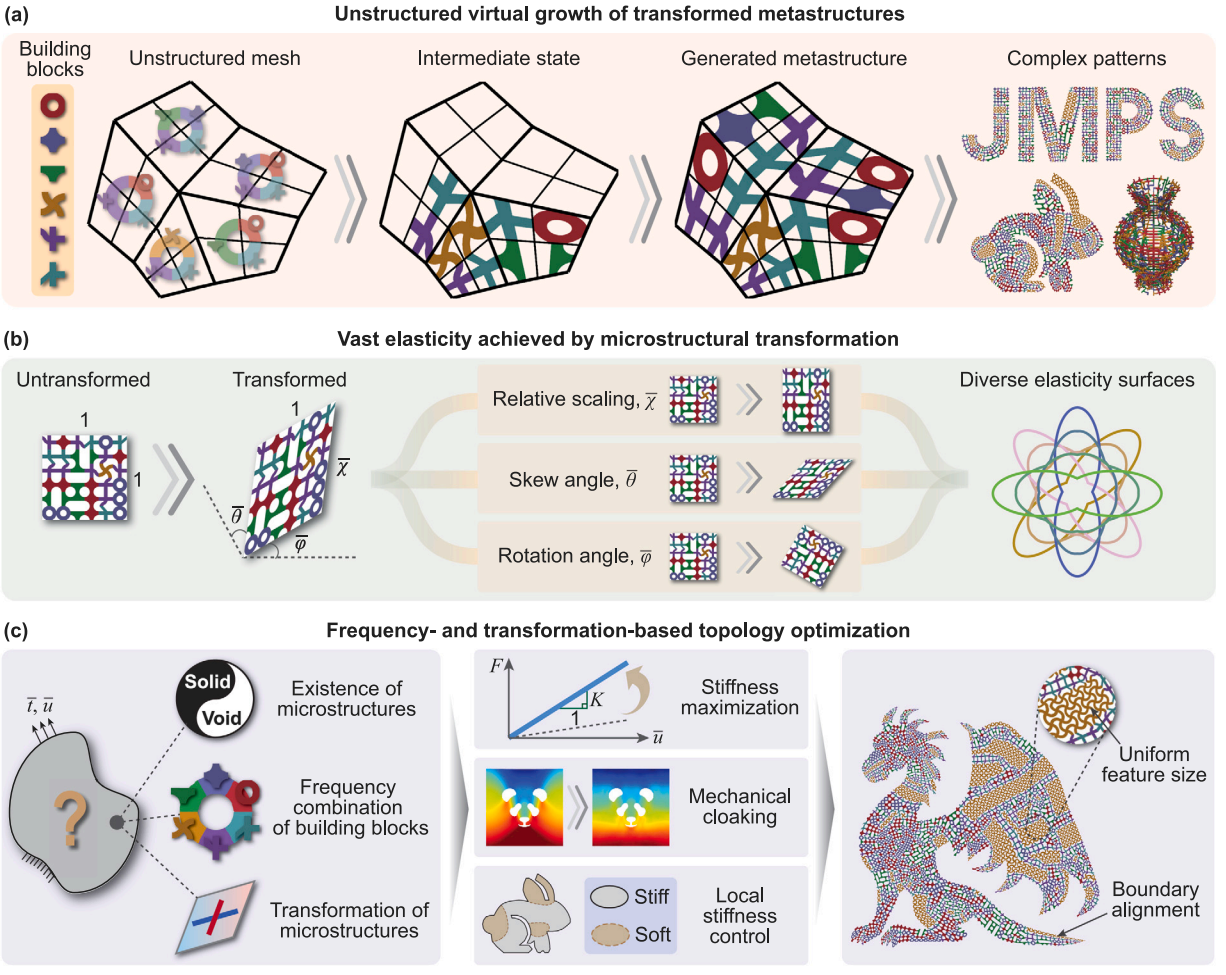

Fig. 1. Unstructured virtual growth of irregular architectures for optimized metastructures. (a) Unstructured virtual growth for generating metastructures. (b) Vast elasticity achieved by microstructural transformation. (c) Frequency- and transformation-based topology optimization for discovering optimized metastructures. The variables $\bar{t}$ and $\bar{u}$ are the amplitudes of the applied traction and displacement loadings, respectively. The variable F is the resultant reaction force, and K is the structural stiffness.

2022) and extended[1] (Jia et al., 2024a,b) virtual growth algorithms and detail their key differences compared to the proposed scheme.

The classical virtual growth algorithm (Liu et al., 2022) is a graphical theory designed to create aperiodic and stochastic patterns by tiling predefined building blocks on a structured mesh. These patterns ensure seamless integration (no dangling parts) among neighboring building blocks based on adjacency rules. Moreover, the distribution of building blocks in the created pattern conforms to the target frequency combination, *i.e.*, the desired proportion of each building block within the mesh. By assigning material constants (*e.g.*, Lamé constants) to the generated patterns, we can create a wide spectrum of metamaterials with diverse homogenized properties (Liu et al., 2022; Magrini et al., 2024).

Recently, the classical virtual growth algorithm has been extended in Jia et al. (2024a,b) to accommodate heterogeneous frequency combinations, wherein the desired proportion of each building block varies spatially. Building upon this extended virtual growth algorithm, the work in Jia et al. (2024a,b) introduces generative computational frameworks and successfully derives optimized metamaterials and metastructures with diverse target responses. However, the performance of these optimized designs can be further enhanced, as the building blocks are strictly arranged in horizontal and vertical directions. This confinement stems from the reliance on a structured mesh in the extended virtual growth algorithm, which can be traced back to the classical version in Liu et al. (2022).

To fill building blocks within an unstructured mesh, we propose the unstructured virtual growth algorithm, aimed at generating transformed metamaterials and metastructures. Compared to the extended virtual growth algorithm in Jia et al. (2024a,b), the

[1] Open-source code is available in GitHub at https://github.com/missionlab/Heterogeneous-Virtual-Growth.

unstructured version has three key differences. First, the unstructured virtual growth algorithm incorporates a wider array of representative building blocks, including rotationally symmetric and asymmetric ones. Second, to handle the complex topological relationships among cells within the unstructured mesh, the unstructured virtual growth algorithm uses a cell connectivity matrix to effectively identify the neighbors of each cell. Finally, during the virtual growth process, the unstructured virtual growth algorithm converts the unstructured mesh into an abstract vector to efficiently fill building blocks and store the information of filled ones. These key differences are detailed below.

2.1. Preparing building blocks

To generate metastructures using the virtual growth algorithm, we need to prescribe simple yet representative building blocks (Fig. 2(a)). We emphasize that the only stringent requirement for building blocks is that each building block must be capable of connecting to at least one of the other building blocks. As long as this condition is met, we have the freedom to select building block geometries, which can be directly specified, inspired by known patterns, or optimized through an inverse design problem.

Despite the flexibility in selecting building blocks, several guiding principles are recommended. First, to maximize structural responses such as stiffness (as discussed in Section 5.1), biaxially symmetric building blocks are preferred because they create the shortest load paths (see Fig. 8(b) of Jia et al. (2024b)). Second, to tailor structural responses to various target values (rather than merely maximizing or minimizing them; as discussed in Section 5.2), a combination of diverse building blocks — with different connecting positions and directions — is preferred, as it achieves a wider range of homogenized material properties. Finally, incorporating building blocks with more than three connecting directions (in 2D) can enhance the convergence of the virtual growth algorithm by increasing the likelihood of finding admissible building blocks.

In this study, we directly specify the building block geometries for simplicity and deliberately select building blocks different from previous studies (Liu et al., 2022; Jia et al., 2024a,b; Magrini et al., 2024) to demonstrate the flexibility in choosing building blocks. Compared to previous work that primarily utilizes axially symmetric building blocks, we extend our approach to incorporate rotationally symmetric and asymmetric ones. As shown in Fig. 2(a), we include three axially symmetric (`ring`, `cross`, and `letter T`), one rotationally symmetric (`letter X`), and two asymmetric (`irregular 1` and `irregular 2`) building blocks. Moreover, existing research mainly uses slender building blocks that can only be connected in the middle. As a result, the generated designs resemble trusses that could also be obtained through alternative design techniques. On the contrary, the building blocks employed here exhibit more irregular geometries, and we allow them to be connected through corners. Consequently, the created metastructures are characterized by a more free-form and organic aesthetic.

After defining the building blocks, our next objective is to identify their unique variations. Following the approach outlined in Liu et al. (2022) and Jia et al. (2024a,b), we rotate each building block by 0, $\pi/2$, π, and $3\pi/2$ (instead of allowing arbitrary rotations, as will be introduced in Section 3) and retain the unique ones. For the newly added rotationally symmetric building block, `letter X`, we also consider its chiral variation to enrich achievable material properties. After identifying the unique variations of building blocks, we discretize them into microscale elements, which will be used in microscale finite element analysis (FEA). Furthermore, we encode these unique building block variations with integers ranging from 1 to M^{var}. Here, the parameter M^{var} is the number of unique variation types ($M^{\text{var}} = 16$ in Fig. 2(a)). These encoded building block variations will be employed in subsequent unstructured virtual growth.

2.2. Preparing the unstructured mesh

Before growing metastructures, we need to prepare an unstructured mesh. As shown in Fig. 2(b), we consider a sample unstructured mesh consisting of five macroscale elements with each element assigned a target frequency combination of building blocks. To fill the building blocks in the mesh, we subdivide each element into four macroscale cells and encode them with unique integers ranging from (1) to (20).

After encoding the cells within the mesh, the next step is to identify the neighbors for each cell. In the classical (Liu et al., 2022) and extended (Jia et al., 2024a,b) algorithms, the neighbors of a given cell are simply the closest ones in the top, down, left, and right directions because the mesh is structured. However, for the unstructured mesh considered here, these four directions are ill-defined because the orientations of the cells may not align with the axes of the Cartesian coordinate system. Moreover, an unstructured mesh can contain singularities, where the number of cells connected to one interior node is unequal to four.

To address this challenge, we construct a cell connectivity matrix, D, to track the complex topological relationships among the cells (Fig. 2(b)). Here, $D_{ij} = k$ denotes that the jth edge of cell i is connected to cell k if $k < N^{\text{cell}} + 1$ with N^{cell} representing the number of cells; otherwise, no cells are connected to cell i through edge j. Algorithm 1 outlines the procedure to compute this cell connectivity matrix, which can be implemented in a computer program with vectorization to enhance efficiency.

After deriving the cell connectivity matrix, we abstract the unstructured mesh as a vector (Fig. 2(b)) for the subsequent virtual growth process. The abstract vector reads as

$$\mathcal{G}_{(N^{\text{cell}}+1)\times 1} = [\mathcal{G}_1, \mathcal{G}_2, \dots, \mathcal{G}_{N^{\text{cell}}}, \mathcal{G}_{N^{\text{cell}}+1}]^{\top},$$

with $\mathcal{G}_i \in \{1, 2, \dots, M^{\text{var}}, M^{\text{var}} + 1\}$ for $i = 1, 2, \dots, N^{\text{cell}}$ and $\mathcal{G}_{N^{\text{cell}}+1} = M^{\text{var}} + 2$. The expression $\mathcal{G}_i = k$ for $i = 1, 2, \dots, N^{\text{cell}}$ represents that the encoded building block variation k is in cell i if $k < M^{\text{var}} + 1$; otherwise, no building block has been filled in cell i yet. The argument $\mathcal{G}_{N^{\text{cell}}+1} = M^{\text{cell}} + 2$ represents the boundary of the mesh.

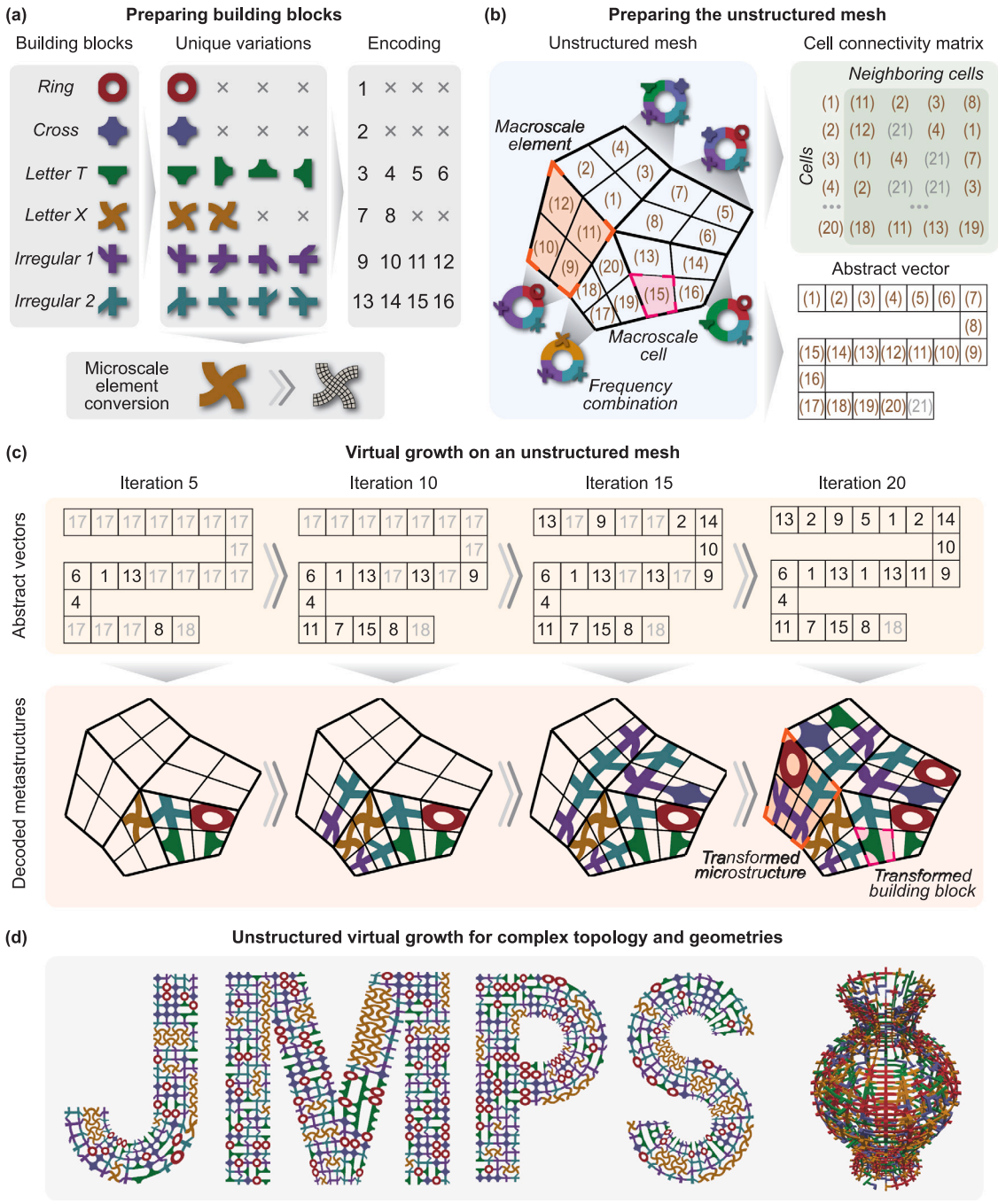

Fig. 2. Proposed unstructured virtual growth algorithm. (a) Prescribed building blocks, unique variations, and encoding. Rotational variations are considered for all six building blocks while chiral variations are considered for the `Letter X` building block. The bottom box shows the conversion from a building block variation to microscale elements. (b) Preparation of the unstructured mesh. The unstructured mesh consists of 5 macroscale elements with each further divided into 4 macroscale cells (20 cells in total). Each macroscale element is assigned a target frequency combination of building blocks in (a). The numbers in parentheses represent the cell numbering, and number (21) represents the mesh boundary. The right boxes in (b) illustrate the cell connectivity matrix and abstract vector derived from the given mesh. (c) Virtual growth on an unstructured mesh. The top row shows the abstract vectors with the numbers representing the numbering of filled building block variations. Number 17 represents that no building block is filled, and number 18 implies the wall at the mesh boundary. The bottom row shows the decoded metastructures. (d) Unstructured virtual growth for complex topology and geometries in 2D and 3D.

Algorithm 1: Computing the cell connectivity matrix (D)

Inputs: the number of cells, N^{cell}; the number of nodes (edges) in one cell, N^{node}; cell construction matrix, $C_{N^{\text{cell}}\times N^{\text{node}}}$ with C_{ij} representing the jth node number of cell i;
Compute the augmented cell construction matrix, $\overline{C}_{N^{\text{cell}}\times(N^{\text{node}}+1)} \leftarrow [C, C_{*1}]$, where C_{*1} represents the first column of C;
Initialize the primary cell counter, $i \leftarrow 1$;
Initialize the cell connectivity matrix, $D_{N^{\text{cell}}\times N^{\text{node}}}$, with all components equal to $N^{\text{cell}}+1$;
for $i \le N^{cell}$ **do**
  Initialize the edge counter of the primary cell, $j \leftarrow 1$;
  for $j \le N^{node}$ **do**
    Identify the node numbers that form edge j of primary cell i, $\mathbb{E}^{[ij]} \leftarrow \{\overline{C}_{i,j}, \overline{C}_{i,j+1}\}$;
    Initialize the query cell counter, $k \leftarrow 1$;
    for $k \le N^{cell}$ **do**
      Initialize the edge counter of the query cell, $l \leftarrow 1$;
      for $l \le N^{node}$ **do**
        Identify the node numbers that form edge l of query cell k, $\mathbb{E}^{[kl]} \leftarrow \{\overline{C}_{k,l}, \overline{C}_{k,l+1}\}$;
        if $\mathbb{E}^{[ij]} = \mathbb{E}^{[kl]}$ **then**
          Update the cell connectivity matrix, $D_{ij} \leftarrow k$;
          Break;
        end
      end
      if $D_{ij} = k$ **then**
        Break;
      end
    end
  end
end

2.3. Growing transformed metastructures

Upon finishing the preparation of building blocks (Fig. 2(a)) and the unstructured mesh (Fig. 2(b)), we are ready to grow transformed metastructures. The goal is to fill each macroscale cell with one building block such that

- the filled building blocks are transformed through scaling, skew, and rotation to accommodate the cell geometries,
- the neighboring building blocks satisfy adjacency rules (see Appendix A for details) — being fully connected or detached (no dangling parts),
- and the building block distribution in each macroscale element adheres to the assigned frequency combination.

To achieve these requirements, we adopt an encoding–decoding scheme as follows. Initially, we assign $\mathcal{G}_1$–$\mathcal{G}_{N^{\text{cell}}}$ as $M^{\text{var}}+1$ to represent an empty mesh without any filled building blocks. We then identify the neighbors for each cell within the mesh and determine the building blocks in those neighboring cells (empty so far) based on the cell connectivity matrix (D) and abstract vector ($\mathcal{G}$). Specifically, cell i's neighbors are $D_{i,1}$–$D_{i,N^{\text{node}}}$, and therefore the neighboring building blocks are $\mathcal{G}_{D_{i,1}}$–$\mathcal{G}_{D_{i,N^{\text{node}}}}$. Once obtaining the neighboring building blocks, we identify admissible building blocks for cell i based on adjacency rules in Appendix A.

Upon deriving the admissible building blocks for each cell within the mesh, we finish the remaining steps by following Jia et al. (2024a,b). Specifically, for each cell, we compute the normalized probabilities of picking each admissible building block and then compute the cell's entropy. We then select the cell with the least entropy and fill in one admissible building block based on the normalized probabilities. We repeat the above procedure until each cell is filled with one building block. Eventually, the abstract vector satisfies $\mathcal{G}_i \in \{1, 2, \dots, M^{\text{var}}\}$ for $i = 1, 2, \dots, N^{\text{cell}}$, and we decode the integers, 1–M^{var}, to the building block variations and generate the desired metastructure (Fig. 2(c)).

We highlight that the generated metastructure is an ensemble of seamlessly connected transformed microstructures, and these microstructures further consist of transformed building blocks with an explicitly controllable and globally uniform feature size (Fig. 2(c)). In addition, as shown in Fig. 2(d), the proposed unstructured virtual growth algorithm applies to various meshes with complex topology and geometries, and it can be easily generalized to create 3D metastructures.

3. Frequency-controlled and transformed homogenized elasticity

In this section, we focus on another important part of the proposed methodology — frequency-controlled and transformed homogenized elasticity. Specifically, we aim to determine the influence of the frequency combination of building blocks and the transformation (scaling, skew, and rotation) of microstructure on the homogenized elasticity matrix. To derive this constitutive

relationship, we begin by exploring the interplay between the frequency combination of the building blocks and the homogenized elasticity. Next, we prove that homogenized elasticity depends on the relative scaling rather than the absolute values. Subsequently, we elucidate the relationship between the microstructural transformation and the homogenized elasticity. Finally, we present simple verification to examine the derived relationships.

3.1. Microstructural elasticity determined by frequency combination

To derive the relationship between the frequency combination of building blocks and the homogenized elasticity of the resulting microstructure, we adopt a data-driven approach by following Jia et al. (2024a,b). First, we construct a material database comprising $N^{\mathtt{data}}$ data points. Each data point includes one frequency combination, $\{\overline{\xi}_1, \overline{\xi}_2, \dots, \overline{\xi}_{M^{\mathtt{freq}}}\}$ ($M^{\mathtt{freq}}$ denotes the number of frequency variables), along with $N^{\mathtt{sample}}$ sample microstructures generated based on the same frequency combination (recall the virtual growth algorithm is stochastic). Next, we employ numerical homogenization (Vigliotti and Pasini, 2012) (the key steps are summarized in Appendix B) to evaluate homogenized elasticity matrices for all sample microstructures. We then compute the average elasticity matrix for sample microstructures corresponding to the same frequency combination. This process yields $N^{\mathtt{data}}$ frequency combination–elasticity matrix pairs, eventually establishing a relationship between the frequency combination and the average elasticity matrix. In doing so, we assume that the homogenized elasticity follows a normal distribution with unimodality and near-zero skewness (see numerical verification in Jia et al. (2024a)), and we focus on the expected value of the material properties.

The frequency combination–elasticity matrix pairs derived above are discrete. However, the subsequent topology optimization requires a continuous and differentiable relationship to use the gradient-based optimizer. To obtain this relationship, we train a fully connected neural network based on the discrete data. This neural network takes the frequency combination as input and outputs the independent components of the elasticity matrix. In this neural network model, we use the rectified linear unit (ReLU) as a nonlinear activation function, and the mathematical expressions of the neural network read as

$$\mathbf{h}_1 = \mathbf{W}_1\overline{\boldsymbol{\xi}} + \mathbf{b}_1, \quad \overline{\mathbf{h}}_1 = \mathrm{ReLU}(\mathbf{h}_1), \quad \mathbf{h}_2 = \mathbf{W}_2\overline{\mathbf{h}}_1 + \mathbf{b}_2, \quad \overline{\mathbf{h}}_2 = \mathrm{ReLU}(\mathbf{h}_2), \quad \text{and} \quad \mathbf{c} = \mathbf{W}_3\overline{\mathbf{h}}_2 + \mathbf{b}_3. \tag{1}$$

Here, the vector $\overline{\boldsymbol{\xi}} = [\overline{\xi}_1, \overline{\xi}_2, \dots, \overline{\xi}_{M^{\mathtt{freq}}}]^\top$ represents the input frequency combination, and the vector $\mathbf{c}$ denotes the independent components of the elasticity matrix. The operator $\overline{\mathbf{v}} = \mathrm{ReLU}(\mathbf{v})$ is defined as $\overline{v}_i = \max\{0, v_i\}$ for a dummy vector, $\mathbf{v}$. The matrices $\mathbf{W}_1$–$\mathbf{W}_3$ and bias vectors $\mathbf{b}_1$–$\mathbf{b}_3$ consists of neural network parameters to be optimized. To determine these matrices and bias vectors, we utilize the Adam optimizer (Kingma and Ba, 2017) to minimize the mean squared error between the predicted and true values of the elasticity components. Based on the trained neural network, we establish a continuous and differentiable relationship between the frequency combination of building blocks and the homogenized elasticity matrix of the microstructure. In Section 3.3, we further expand this neural network to account for microstructural transformations.

3.2. Invariance of microstructural elasticity under uniform scaling

After determining the interplay between the frequency combination of building blocks and microstructural elasticity, we shift our focus to how microstructural elasticity is influenced by transformations. As shown in Fig. 3, a given microstructure can be sequentially transformed through relative scaling ($\overline{\chi}$), skew ($\overline{\theta}$), and rotation ($\overline{\varphi}$). In this section, we focus on the first step and demonstrate that microstructural elasticity depends only on the relative scaling ($\overline{\chi}$) instead of the absolute values (see a similar statement in Ma et al. (2021)).

Based on the homogenization theory in Vigliotti and Pasini (2012) (summarized in Appendix B), the homogenized elasticity matrix of a unit cell (or a microstructure in this context) is expressed as

$$\mathbf{D}_{\mathtt{H}} = \frac{1}{V}\mathbf{B}_\varepsilon^\top \mathbf{K}_{\Delta\mathbf{a}} \mathbf{B}_\varepsilon,$$

where $\mathbf{K}_{\Delta\mathbf{a}} = \mathbf{D}_a^\top \mathbf{K}_{\mathtt{m}} \mathbf{D}_a$, $\mathbf{D}_a = \mathbf{B}_0\mathbf{D}_0 + \mathbf{B}_a$, and $\mathbf{D}_0 = -(\mathbf{B}_0^\top \mathbf{K}_{\mathtt{m}} \mathbf{B}_0)^+ \mathbf{B}_0^\top \mathbf{K}_{\mathtt{m}} \mathbf{B}_a$. In these expressions, $\mathbf{K}_{\mathtt{m}}$ is the global stiffness matrix at the microscale. Topological matrices $\mathbf{B}_0$ and $\mathbf{B}_a$ define the relationships between all degrees of freedom (DOFs) and the independent DOFs as well as the changes of periodic vectors of the microstructure. Matrix $\mathbf{B}_\varepsilon$ relates the macroscale strain to the changes of periodic vectors. The variable V stands for the macroscopic area in 2D and volume in 3D.

We now evaluate the transformed homogenized elasticity matrices ($\mathbf{D}'_{\mathtt{H}}$ in 2D and $\mathbf{D}''_{\mathtt{H}}$ in 3D) under uniform scaling with a parameter $s > 0$. The transformation rule reads as $\mathbf{x} = s\mathbf{X}$. The variables $\mathbf{X} \in \mathbb{R}^{\mathtt{sd}}$ and $\mathbf{x} \in \mathbb{R}^{\mathtt{sd}}$ represent the material points before and after transformation, respectively, and $\mathtt{sd} \in \{2, 3\}$ is the spatial dimension. To evaluate $\mathbf{D}'_{\mathtt{H}}$ and $\mathbf{D}''_{\mathtt{H}}$, we begin by deriving the transformed global stiffness matrices (see the derivation in Appendix C) as

$$\mathbf{K}'_{\mathtt{m}} = \mathbf{K}_{\mathtt{m}} \text{ in 2D} \quad \text{and} \quad \mathbf{K}''_{\mathtt{m}} = s\mathbf{K}_{\mathtt{m}} \text{ in 3D}.$$

Next, we compute the $\mathbf{D}_0$ matrices after transformation ($\mathbf{D}'_0$ in 2D and $\mathbf{D}''_0$ in 3D) as

$$\begin{cases} \mathbf{D}'_0 = -(\mathbf{B}_0'^\top \mathbf{K}'_{\mathtt{m}} \mathbf{B}'_0)^+ \mathbf{B}_0'^\top \mathbf{K}'_{\mathtt{m}} \mathbf{B}'_a = -(\mathbf{B}_0^\top \mathbf{K}_{\mathtt{m}} \mathbf{B}_0)^+ \mathbf{B}_0^\top \mathbf{K}_{\mathtt{m}} \mathbf{B}_a = \mathbf{D}_0 & \text{in 2D;} \\ \mathbf{D}''_0 = -(\mathbf{B}_0''^\top \mathbf{K}''_{\mathtt{m}} \mathbf{B}''_0)^+ \mathbf{B}_0''^\top \mathbf{K}''_{\mathtt{m}} \mathbf{B}''_a = -[\mathbf{B}_0^\top (s\mathbf{K}_{\mathtt{m}}) \mathbf{B}_0]^+ \mathbf{B}_0^\top (s\mathbf{K}_{\mathtt{m}}) \mathbf{B}_a = \mathbf{D}_0 & \text{in 3D.} \end{cases}$$

Here, we use the fact that uniform scaling does not change the topological relationships among DOFs (*i.e.*, $\mathbf{B}'_0 = \mathbf{B}''_0 = \mathbf{B}_0$ and $\mathbf{B}'_a = \mathbf{B}''_a = \mathbf{B}_a$).

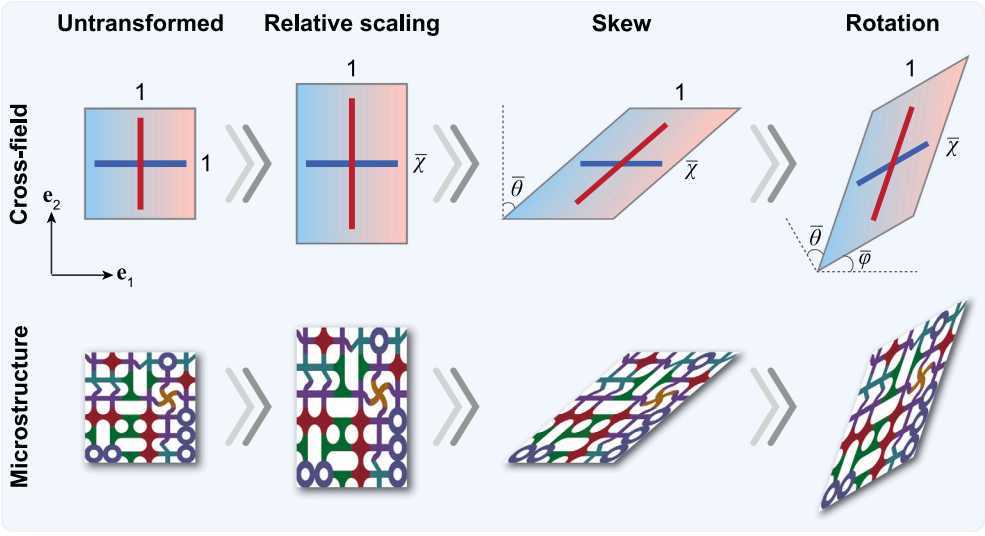

Fig. 3. Illustration of transformation variables. The top row presents cross-field representations, while the bottom row illustrates the corresponding microstructural transformations. In the cross-field representation, the length ratio of the two line segments indicates the relative scaling ($\overline{\chi}$), while the orientations of the line segments depict the skew ($\overline{\theta}$) and rotation ($\overline{\varphi}$) angles.

Subsequently, we compute transformed $\mathbf{D}_a$ matrices as

$$\mathbf{D}'_a = \mathbf{B}'_0\mathbf{D}'_0 + \mathbf{B}'_a = \mathbf{D}_a \text{ in 2D} \quad \text{and} \quad \mathbf{D}''_a = \mathbf{B}''_0\mathbf{D}''_0 + \mathbf{B}''_a = \mathbf{D}_a \text{ in 3D}$$

as well as transformed $\mathbf{K}_{\Delta\mathbf{a}}$ matrices as

$$\mathbf{K}'_{\Delta\mathbf{a}} = \mathbf{D}'^{\top}_a\mathbf{K}'_{\mathbb{m}}\mathbf{D}'_a = \mathbf{K}_{\Delta\mathbf{a}} \text{ in 2D} \quad \text{and} \quad \mathbf{K}''_{\Delta\mathbf{a}} = \mathbf{D}''^{\top}_a\mathbf{K}''_{\mathbb{m}}\mathbf{D}''_a = s\mathbf{K}_{\Delta\mathbf{a}} \text{ in 3D.}$$

Finally, we derive the transformed homogenized elasticity matrices as

$$\begin{cases} \mathbf{D}'_{\mathrm{H}} = \dfrac{1}{V'}\mathbf{B}'^{\top}_{\varepsilon}\mathbf{K}'_{\Delta\mathbf{a}}\mathbf{B}'_{\varepsilon} = \dfrac{1}{s^2V}(s\mathbf{B}_{\varepsilon})^{\top}\mathbf{K}_{\Delta\mathbf{a}}(s\mathbf{B}_{\varepsilon}) = \mathbf{D}_{\mathrm{H}} & \text{in 2D;} \\ \mathbf{D}''_{\mathrm{H}} = \dfrac{1}{V''}\mathbf{B}''^{\top}_{\varepsilon}\mathbf{K}''_{\Delta\mathbf{a}}\mathbf{B}''_{\varepsilon} = \dfrac{1}{s^3V}(s\mathbf{B}_{\varepsilon})^{\top}(s\mathbf{K}_{\Delta\mathbf{a}})(s\mathbf{B}_{\varepsilon}) = \mathbf{D}_{\mathrm{H}} & \text{in 3D.} \end{cases} \tag{2}$$

Here, $V' = s^2V$ and $V'' = s^3V$ represent the macroscopic area in 2D and volume in 3D after uniform scaling, respectively. Moreover, the matrix $\mathbf{B}_{\varepsilon}$ becomes $\mathbf{B}'_{\varepsilon} = s\mathbf{B}_{\varepsilon}$ in 2D and $\mathbf{B}''_{\varepsilon} = s\mathbf{B}_{\varepsilon}$ in 3D after transformation. Eq. (2) shows that the homogenized elasticity matrix remains unchanged in both 2D and 3D when the microstructure undergoes uniform scaling (instead of deformation). Therefore, the transformed elasticity depends only on the relative scaling ($\overline{\chi}$), and we can condense the design variables in the subsequent analyses.

3.3. Microstructural elasticity determined by transformation

Based on the previous analysis, microstructural elasticity is controlled by the frequency combination of building blocks and the transformation of microstructure, and the latter includes relative scaling ($\overline{\chi}$), skew ($\overline{\theta}$), and rotation ($\overline{\varphi}$). In this section, we derive the resultant homogenized elasticity matrix that accounts for all these variables.

To determine the relationship between the elasticity matrix and relative scaling ($\overline{\chi}$) as well as the skew angle ($\overline{\theta}$), we can generalize the neural network model in (1). Specifically, we augment the input vector in (1) to include the relative scaling and the skew angle. The mathematical expressions of the augmented neural network read as

$$\mathbf{h}_1 = \mathbf{W}'_1\overline{\mathbf{v}} + \mathbf{b}'_1, \quad \overline{\mathbf{h}}_1 = \mathrm{ReLU}(\mathbf{h}_1), \quad \mathbf{h}_2 = \mathbf{W}'_2\overline{\mathbf{h}}_1 + \mathbf{b}'_2, \quad \overline{\mathbf{h}}_2 = \mathrm{ReLU}(\mathbf{h}_2), \quad \text{and} \quad \mathbf{c} = \mathbf{W}'_3\overline{\mathbf{h}}_2 + \mathbf{b}'_3, \tag{3}$$

where the parameters with a prime represent the updated matrices and vectors in the augmented neural network. The variable $\overline{\mathbf{v}} = [\overline{\xi}_1, \overline{\xi}_2, \ldots, \overline{\xi}_{M^{\mathrm{freq}}}, \widetilde{\chi}, \widetilde{\theta}]^{\top}$ is the augmented input vector. Here, to scale all input variables to [0, 1], we use the filtered relative scaling ($\widetilde{\chi} \in [0,1]$) and skew angle ($\widetilde{\theta} \in [0,1]$) rather than the physical ones ($\overline{\chi}$ and $\overline{\theta}$). More details on the filtered variables are provided in Section 4.

To generate the train data for this augmented neural network, we uniformly sample N^{data} data points such that each data point consists of

- a frequency combination ($\{\overline{\xi}_1, \overline{\xi}_2, \ldots, \overline{\xi}_{M^{\mathrm{freq}}}\}$) sampled from the hyperplane $\sum_{i=1}^{M^{\mathrm{freq}}} \overline{\xi}_i = 1$ subjected to $\overline{\xi}_i \in [0,1]$ for $i = 1, 2, \ldots, M^{\mathrm{freq}}$,

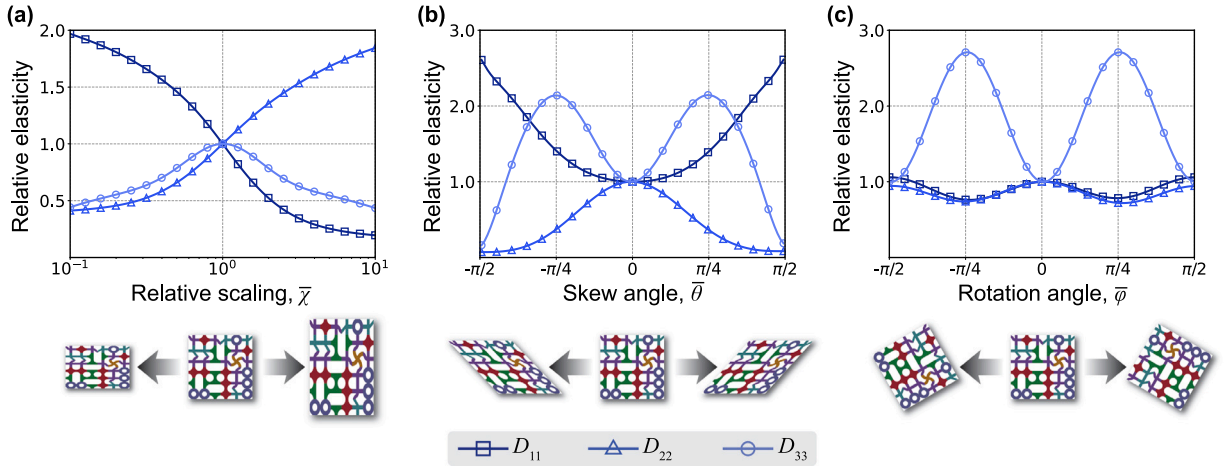

Fig. 4. Relative values of transformed elasticity under varying (a) relative scaling, (b) skew angles, and (c) rotations angles.

- a filtered relative scaling parameter ($\widetilde{\chi}$) sampled from [0, 1],
- and a filtered skew angle ($\widetilde{\theta}$) also sampled from [0, 1].

The remaining procedure mirrors Section 3.1 except that the homogenized elasticity matrix is evaluated in the transformed configuration controlled by the physical relative scaling ($\overline{\chi}$) and skew angle ($\overline{\theta}$).

Following the procedure in Section 3.1, we train the augmented neural network and derive the transformed elasticity matrix as

$$\mathbf{D}_{\mathrm{t}}(\bar{\xi}_1, \bar{\xi}_2, \ldots, \bar{\xi}_{M^{\mathrm{freq}}}; \widetilde{\chi}, \widetilde{\theta}, \widetilde{\varphi}) = \mathbf{T}(\overline{\varphi}(\widetilde{\varphi}))\mathcal{NN}(\bar{\xi}_1, \bar{\xi}_2, \ldots, \bar{\xi}_{M^{\mathrm{freq}}}; \widetilde{\chi}, \widetilde{\theta})\mathbf{T}^{\top}(\overline{\varphi}(\widetilde{\varphi})). \tag{4}$$

Here, the operator $\mathcal{NN}$ stands for the neural network model whose mathematical prescription is given in (3). This operator accounts for the contributions from the frequency variables ($\bar{\xi}_1, \bar{\xi}_2, \ldots, \bar{\xi}_{M^{\mathrm{freq}}}$), relative scaling ($\widetilde{\chi}$), and skew angle ($\widetilde{\theta}$). Eq. (4) also incorporates the contribution from microstructural rotation by introducing the matrix $\mathbf{T}$ (see the derivation in Appendix D), where the arguments $\widetilde{\varphi} \in [0, 1]$ and $\overline{\varphi}$ are the filtered and physical rotation angles, respectively.

We highlight that the continuous and differentiable relationship in (4) enables us to exploit a broad spectrum of material properties resulting from microstructural transformation. Fig. 4 presents the dependencies between the D_{11}, D_{22}, and D_{33} components (scaled based on the untransformed values) and the relative scaling ($\overline{\chi}$), skew angle ($\overline{\theta}$), and rotation angle ($\overline{\varphi}$). In general, these elasticity components can vary from 0.2 to 3 times the untransformed values, and therefore enlarge the design space in subsequent topology optimization.

3.4. Simple verification

In this section, we perform simple numerical tests to verify the transformed elasticity matrix derived in (4). As shown in Fig. 5(a), we examine four representative metastructures characterized by relative scaling ($\overline{\chi} = 0.5$), skew ($\overline{\theta} = \pi/6$), rotation ($\overline{\varphi} \in [0, \pi/2]$), and nontrivial frequency combination of building blocks ($\bar{\xi}_1 = \bar{\xi}_2 = 0.5$), respectively. Fig. 5(a) also depicts the boundary conditions of these metastructures, and each metastructure is tested under two load cases. Fig. 5(b) and (c) present the comparisons of displacement amplitudes ($|\mathbf{u}|$) between microscale and macroscale (homogenized) analyses under load cases 1 and 2, respectively. These comparisons reveal agreement between the microscale and macroscale displacement fields. Additionally, we compute the strain energy (W) and its relative error (e) for each metastructure under both load cases. The absolute value of the error ($|e|$) remains below 5% across all scenarios, therefore verifying the above analysis for evaluating transformed and frequency-controlled homogenized elasticity.

4. Frequency- and transformation-based topology optimization

Having introduced the unstructured virtual growth algorithm alongside frequency-controlled and transformed homogenized elasticity, we proceed to present the frequency- and transformation-based topology optimization methodology for uncovering transformed metastructures with optimized responses. This methodology comprises four parts: design space parameterization, microstructural elasticity interpolation, topology optimization formulation, and finally transformation-guided mesh generation, which are detailed below.

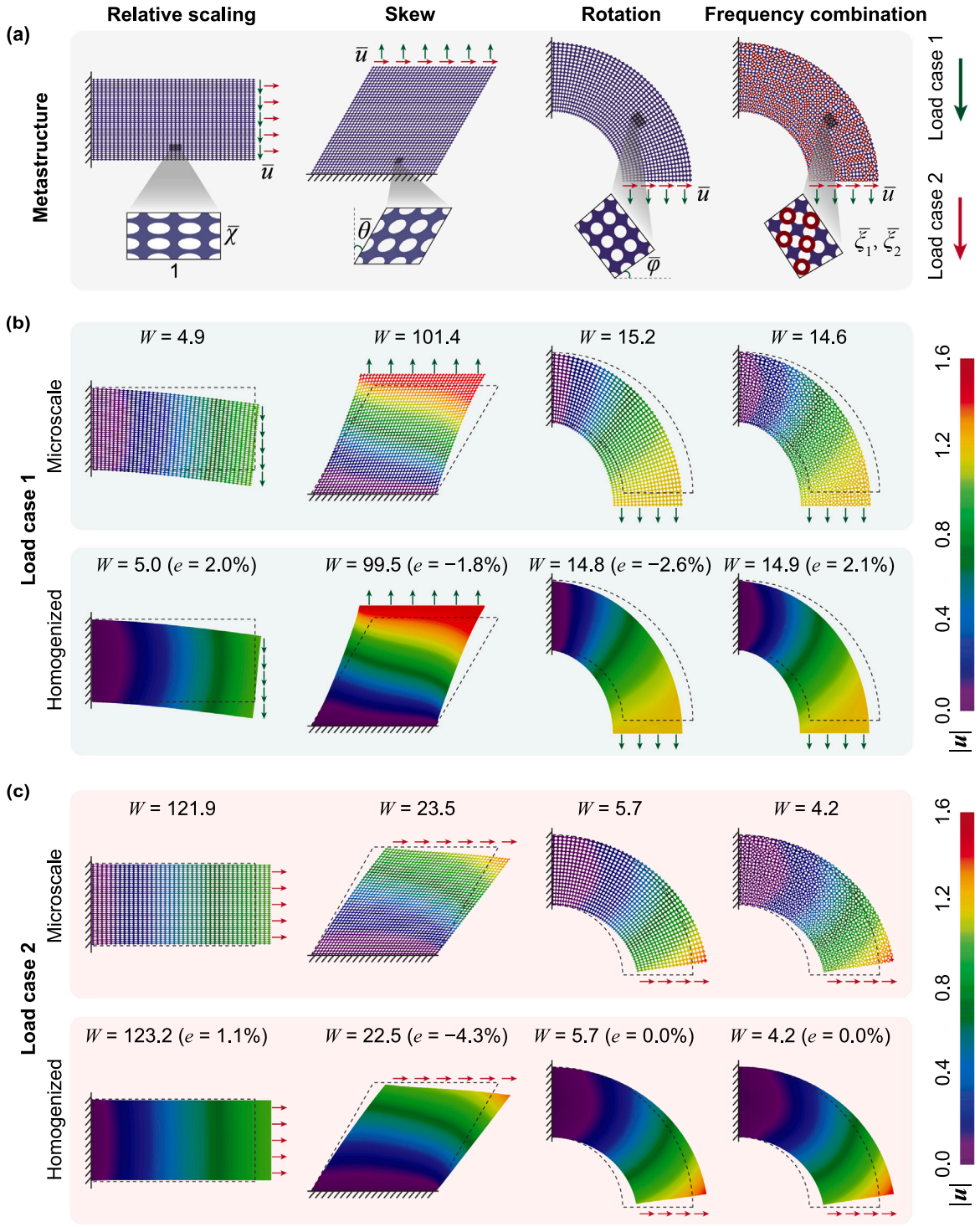

Fig. 5. Verification of transformed and frequency-controlled homogenized elasticity. (a) Metastructures characterized by relative scaling ($\overline{\chi} = 0.5$), skew ($\overline{\theta} = \pi/6$), rotation ($\overline{\varphi} \in [0, \pi/2]$), and nontrivial frequency combination of building blocks ($\overline{\xi}_1 = \overline{\xi}_2 = 0.5$). Each metastructure is tested under two load cases with a displacement loading amplitude set to $\overline{u} = 1$ mm. (b) Comparison of displacement amplitudes ($|\mathbf{u}|$) between microscale and macroscale (homogenized) analyses under load case 1. The variable W is the strain energy (in N · mm), and e is the relative error. (c) Comparison of displacement amplitudes between microscale and macroscale (homogenized) analyses under load case 2.

4.1. Design space parameterization

To proceed with topology optimization (Bendsøe and Kikuchi, 1988; Bendsoe and Sigmund, 2003; Wang et al., 2021), we need to determine the design variables by parameterizing the design space. Specifically, we define three groups of design variables: (a) the density variable, $\rho(\mathbf{X}) \in [0,1]$, (b) the frequency variables, $\xi_i(\mathbf{X}) \in [\varepsilon, 1-\varepsilon] \subseteq [0,1]$ for $i = 1,2,\dots,M^{\text{freq}}$ and some $\varepsilon \in [0, 0.5)$, and (c) the transformation variables, $\chi(\mathbf{X})$, $\theta(\mathbf{X})$, and $\varphi(\mathbf{X}) \in [0,1]$. We will assign physical interpretations to these design variables following the application of the subsequent filtering and projection operations.

To enable the local homogenization of microstructures, we apply a linear filter (Bourdin, 2001)

$$\widetilde{\zeta}(\mathbf{X}) = \frac{\int_{\Omega} w(\mathbf{X},\mathbf{X}')\zeta(\mathbf{X}')\mathrm{d}\mathbf{X}'}{\int_{\Omega} w(\mathbf{X},\mathbf{X}')\mathrm{d}\mathbf{X}'}$$

to all design variables, $\zeta \in \{\rho, \xi_1, \xi_2, \dots, \xi_{M^{\text{freq}}}, \chi, \theta, \varphi\}$. Here, the parameter $w(\mathbf{X},\mathbf{X}') = \max\{0, R - \|\mathbf{X}-\mathbf{X}'\|_2\}$ is a weighting factor, and R is the specified filter radius. The variables $\mathbf{X}$ and $\mathbf{X}'$ are two material points in the design domain (Ω). The filtered variables, $\widetilde{\zeta} \in \{\widetilde{\rho}, \widetilde{\xi}_1, \widetilde{\xi}_2, \dots, \widetilde{\xi}_{M^{\text{freq}}}, \widetilde{\chi}, \widetilde{\theta}, \widetilde{\varphi}\}$, exhibit similar values in nearby regions, respectively. Therefore, the microstructures are locally and asymptotically periodic and can be homogenized.

After applying the linear filter, we employ various projection schemes to these filtered variables as follows. For the filtered density variable, we apply the Heaviside projection (Bendsoe and Sigmund, 2003)

$$\overline{\rho}(\mathbf{X}) = \frac{\tanh(\beta\phi) + \tanh(\beta(\widetilde{\rho}(\mathbf{X}) - \phi))}{\tanh(\beta\phi) + \tanh(\beta(1-\phi))}$$

to ensure a 0–1 solution of the projected density variable, $\overline{\rho}(\mathbf{X})$. Here, the parameter β is a sharpness coefficient, and $\phi = 0.5$ is the projection threshold. For the filtered frequency variables, we apply the normalization projection (Jia et al., 2024b)

$$\overline{\xi}_i(\mathbf{X}) = \frac{\widetilde{\xi}_i(\mathbf{X})}{\sum_{j=1}^{M^{\text{freq}}} \widetilde{\xi}_j(\mathbf{X})} \quad \text{for} \quad i = 1,2,\dots,M^{\text{freq}}$$

to ensure that the projected frequency variables, $\overline{\xi}_i(\mathbf{X})$ for $i = 1,2,\dots,M^{\text{freq}}$, satisfy the second axiom of probability, *i.e.*, $\sum_{i=1}^{M^{\text{freq}}} \overline{\xi}_i(\mathbf{X}) = 1$. For the filtered transformation variables, we scale them to their corresponding physical values as

$$\overline{\chi}(\mathbf{X}) = \widetilde{\chi}(\mathbf{X})(\chi^{\text{u}} - \chi^{\text{l}}) + \chi^{\text{l}}, \quad \overline{\theta}(\mathbf{X}) = \widetilde{\theta}(\mathbf{X})(\theta^{\text{u}} - \theta^{\text{l}}) + \theta^{\text{l}}, \quad \text{and} \quad \overline{\varphi}(\mathbf{X}) = \widetilde{\varphi}(\mathbf{X})(\varphi^{\text{u}} - \varphi^{\text{l}}) + \varphi^{\text{l}}. \tag{5}$$

Here, the parameters χ^{u} and χ^{l} are the upper and lower bounds of the relative scaling of the microstructure, respectively. Parameters θ^{u} and θ^{l} (φ^{u} and φ^{l}) are the counterparts of the skew (rotation) angle.

After applying the above projection operations, we shall now elucidate the physical meanings of the projected variables (also known as physical variables). Specifically, the projected density variable ($\overline{\rho}(\mathbf{X})$) describes the existence of microstructures. One microstructure exists at material point $\mathbf{X}$ if $\overline{\rho}(\mathbf{X}) = 1$, while no microstructure exists if $\overline{\rho}(\mathbf{X}) = 0$. If the microstructure exists, we further employ the projected frequency variables ($\overline{\xi}_i(\mathbf{X})$ for $i = 1,2,\dots,M^{\text{freq}}$) to determine the frequency combination of building blocks forming this microstructure. Finally, we adopt the projected transformation variables, $\overline{\chi}(\mathbf{X})$, $\overline{\theta}(\mathbf{X})$, and $\overline{\varphi}(\mathbf{X})$, to quantify the relative scaling, skew angle, and rotate angle of the microstructure, respectively.

4.2. Microstructural elasticity interpolation

After parameterizing the design space, we proceed to interpolate the microstructural elasticity matrix for continuous values of design variables. Recall Eq. (4) reveals the relationship between the microstructural elasticity matrix ($\mathbf{D}_{\text{t}}$) and frequency ($\overline{\xi}_1, \overline{\xi}_2, \dots, \overline{\xi}_{M^{\text{freq}}}$) as well as transformation ($\widetilde{\chi}$, $\widetilde{\theta}$, and $\widetilde{\varphi}$) variables. We now incorporate the last ingredient — density variable ($\overline{\rho}$) — by applying the modified version of Solid Isotropic Material with Penalization (modified SIMP) scheme (Bendsoe and Sigmund, 2003) to (4). The interpolated elasticity matrix reads as

$$\mathbf{D}(\overline{\rho}; \overline{\xi}_1, \overline{\xi}_2, \dots, \overline{\xi}_{M^{\text{freq}}}; \widetilde{\chi}, \widetilde{\theta}, \widetilde{\varphi}) = \left[\varepsilon + (1-\varepsilon)\overline{\rho}^p\right] \mathbf{D}_{\text{t}}(\overline{\xi}_1, \overline{\xi}_2, \dots, \overline{\xi}_{M^{\text{freq}}}; \widetilde{\chi}, \widetilde{\theta}, \widetilde{\varphi}), \tag{6}$$

where the parameter $\varepsilon = 10^{-6}$ is a small positive number to prevent the singularity of the global stiffness matrix in FEA. The power $p = 3$ is a penalty parameter. The elasticity matrix $\mathbf{D}_{\text{t}}$ is given in (4).

Based on the interpolated elasticity matrix in (6), we formulate the static equilibrium equations as

$$\begin{cases} \text{Div}[\mathbb{C}(\mathbf{D}) : \mathbf{E}] + \overline{\mathbf{b}} = \mathbf{0}, & \mathbf{X} \in \Omega; \\ \mathbf{u} = \overline{\mathbf{u}}, & \mathbf{X} \in \partial\Omega_{\mathcal{D}}; \\ [\mathbb{C}(\mathbf{D}) : \mathbf{E}]\mathbf{N} = \overline{\mathbf{t}}, & \mathbf{X} \in \partial\Omega_{\mathcal{N}}. \end{cases} \tag{7}$$

Here, $\mathbb{C}$ is the interpolated elasticity tensor, and $\mathbf{E} = (\nabla\mathbf{u} + \nabla\mathbf{u}^{\mathsf{T}})/2$ is the infinitesimal strain tensor with $\mathbf{u}$ representing the displacement field. The vectors $\overline{\mathbf{b}}$, $\overline{\mathbf{t}}$, and $\overline{\mathbf{u}}$ are the prescribed body force, traction, and displacement, respectively. The symbol Ω is the design domain, while $\partial\Omega_{\mathcal{D}}$ and $\partial\Omega_{\mathcal{N}}$ are its Dirichlet and Neumann boundaries, respectively. The symbol $\mathbf{N}$ is the unit outward normal vector of $\partial\Omega_{\mathcal{N}}$.

4.3. Topology optimization formulation

Based on the design space parameterization and microstructural elasticity interpolation described above, we propose a topology optimization formulation as

$$\begin{cases} \underset{\rho;\xi_1,\xi_2,\ldots,\xi_{M^{\text{freq}}};\chi,\theta,\varphi}{\text{minimize:}} & : J(\mathbf{u};\overline{\rho};\overline{\xi}_1,\overline{\xi}_2,\ldots,\overline{\xi}_{M^{\text{freq}}};\widetilde{\chi},\widetilde{\theta},\widetilde{\varphi}); \\ \text{subjected to:} & \begin{cases} g = \dfrac{1}{|\Omega|}\displaystyle\int_\Omega \overline{\rho}\mathrm{d}\mathbf{X} - \overline{V} \le 0; \\ \rho,\chi,\theta,\varphi \in [0,1]; \\ \xi_i \in [\varepsilon, 1-\varepsilon] \subseteq [0,1] \quad \text{for} \quad i = 1,2,\ldots,M^{\text{freq}}; \\ \text{Equilibrium equations in (7).} \end{cases} \end{cases} \tag{8}$$

In this formulation, J and g represent the objective and constraint functions, respectively. The parameter $\overline{V} \in (0,1]$ is the allowable volume fraction at the macroscale. We remark that topology optimization is applied to the global system, and it optimizes the distribution of macroscale/homogenized material properties by identifying the optimal and spatially varying microstructural existence ($\overline{\rho}$), building block combinations ($\overline{\xi}_1$–$\overline{\xi}_{M^{\text{freq}}}$), and microstructural transformations ($\widetilde{\chi}$, $\widetilde{\theta}$, and $\widetilde{\varphi}$). After optimizing these global-level variables, we actualize the metastructures using the optimized variables and the unstructured virtual growth algorithm proposed in Section 2, which locally ensures seamless integration among prescribed building blocks.

Following Jia et al. (2024b), we revisit three representative objective functions in this work, including global stiffness maximization, mechanical cloaking (by programming the displacement field to target values), and local stiffness control (by minimizing/maximizing local strain energy density). To maximize global stiffness under displacement loading (Section 5.1), we define

$$J = -\frac{1}{2}\int_\Omega \mathbf{E} : \mathbb{C} : \mathbf{E}\mathrm{d}\mathbf{X}. \tag{9}$$

To program the displacement field to target values for mechanical cloaking (Section 5.2), we specify

$$J = \sum_{n=1}^{N^{\text{lc}}} \|\mathbf{L}_U^{[n]} \odot (\mathbf{U}^{[n]} - \overline{\mathbf{U}}^{[n]})\|_2^2, \tag{10}$$

where $\mathbf{U}$ is the actual global displacement vector, and $\overline{\mathbf{U}}$ is the target one. The vector $\mathbf{L}_U$ is an indicator such that $L_{U,i} = 1$ if DOF i is controlled and $L_{U,i} = 0$ otherwise. The operator $\odot$ stands for the elementwise product. The superscript $[n]$ is the load case count, and N^{lc} is the number of load cases. To control the local stiffness under body force loading (Section 5.3), we utilize

$$J = W_{\texttt{stiff}} - W_{\texttt{soft}} = \frac{1}{2}\int_{\Omega_{\texttt{stiff}}} \mathbf{E} : \mathbb{C} : \mathbf{E}\mathrm{d}\mathbf{X} - \frac{1}{2}\int_{\Omega_{\texttt{soft}}} \mathbf{E} : \mathbb{C} : \mathbf{E}\mathrm{d}\mathbf{X}, \tag{11}$$

where $\Omega_{\texttt{stiff}} \subseteq \Omega$ and $\Omega_{\texttt{soft}} \subseteq \Omega$ are the subsets of the design domain aimed to be stiff and soft, respectively. The variables $W_{\texttt{stiff}}$ and $W_{\texttt{soft}}$ are the strain energies in $\Omega_{\texttt{stiff}}$ and $\Omega_{\texttt{soft}}$, respectively.

To solve the topology optimization problem in (8), we employ the method of moving asymptotes (MMA) (Svanberg, 1987) to iteratively update the design variables. The MMA optimizer requires the sensitivities of the objective and constraint functions with respect to the design variables. We compute these sensitivities by employing the adjoint method (Bendsoe and Sigmund, 2003) and the automatic differentiation provided by FEniCSx (Baratta et al., 2023) and PyTorch (Ketkar et al., 2021) software. The detailed sensitivity analysis and its verification are given in Appendix E.

4.4. Transformation-guided mesh generation

Once the topology optimization problem in (8) is solved, we derive the optimized transformation variables ($\widetilde{\chi}$, $\widetilde{\theta}$, and $\widetilde{\varphi}$), or equivalently, their projected versions ($\overline{\chi}$, $\overline{\theta}$, and $\overline{\varphi}$) in (5). One immediate task is to generate a mesh such that the geometries of all finite elements conform to the optimized transformation fields. We will use this generated mesh to grow building blocks and create the final metastructure. In this subsection, we introduce the transformation-guided mesh generation that consists of two steps: global parameterization and mesh extraction, which are laid out below.

4.4.1. Global parameterization

The first step in generating a transformation-guided mesh is global parameterization. As shown in Fig. 6, we parameterize the design domain (Ω) with two scalar field variables, $r(\mathbf{X})$ and $s(\mathbf{X})$, such that their isoparametric waves (contours sharing the same r or s values) form the target mesh. To identify desired $r(\mathbf{X})$ and $s(\mathbf{X})$, we follow Bommes et al. (2009) and minimize the quadratic transformation energy defined as

$$\begin{cases} W_{\text{t}}(r,s) = \displaystyle\int_\Omega \left\| \overline{\chi}\cos(\overline{\theta})\nabla r - \text{rot}^+[\overline{\mathbf{r}}(\overline{\varphi})] \right\|_2^2 \mathrm{d}\mathbf{X} + \int_\Omega \left\| \cos(\overline{\theta})\nabla s - \text{rot}^-[\overline{\mathbf{s}}(\overline{\theta},\overline{\varphi})] \right\|_2^2 \mathrm{d}\mathbf{X} \\ \text{subjected to } r(\mathbf{X}_0) = 0 \text{ and } s(\mathbf{X}_0) = 0 \text{ for a dummy } \mathbf{X}_0 \in \Omega. \end{cases} \tag{12}$$

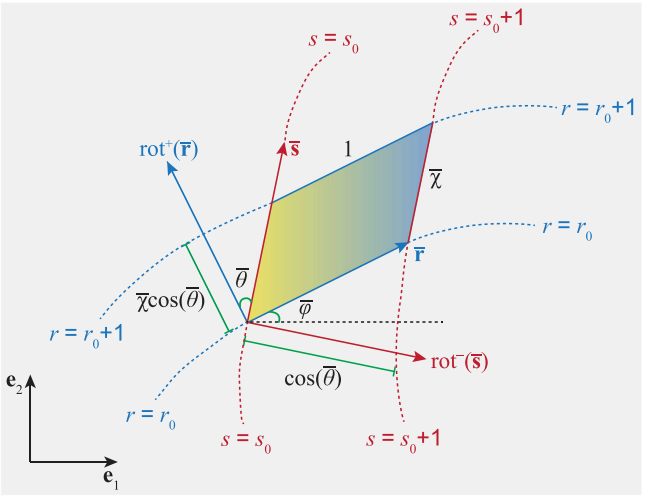

Fig. 6. Illustration of global parameterization. The isoparametric waves of the r and s fields collectively form an approximated parallelogram. The size and orientation of the parallelogram adhere to the optimized transformation variables ($\bar{\chi}$, $\bar{\theta}$, and $\bar{\varphi}$). The parameters r_0 and s_0 are two dummy values.

Here, the vectors $\bar{\mathbf{r}}$ and $\bar{\mathbf{s}}$ are unit cross-field vectors determined by skew ($\bar{\theta}$) and rotation ($\bar{\varphi}$) angles, which are given as

$$\bar{\mathbf{r}}(\bar{\varphi}) = [\cos(\bar{\varphi}), \sin(\bar{\varphi})]^\top \quad \text{and} \quad \bar{\mathbf{s}}(\bar{\theta}, \bar{\varphi}) = [\sin(\bar{\theta} - \bar{\varphi}), \cos(\bar{\theta} - \bar{\varphi})]^\top.$$

The operators rot^+ and rot^- represent rotating a vector counterclockwise and clockwise by $\pi/2$, respectively. Compared to Bommes et al. (2009), we remove the orthogonality requirement between $\bar{\mathbf{r}}$ and $\bar{\mathbf{s}}$ (*i.e.*, the skew angle $\bar{\theta}$ can be nonzero). In addition, we allow the spacing of isoparametric waves to be spatially varying and controlled by relative scaling ($\bar{\chi}$) and skew angle ($\bar{\theta}$).

By analyzing (12), we observe that the gradients of the minimizers, ∇r^* and ∇s^*, align with the directions of $\mathrm{rot}^+(\bar{\mathbf{r}})$ and $\mathrm{rot}^-(\bar{\mathbf{s}})$, respectively. It implies that the isoparametric waves of r^* and s^* are collinear with $\bar{\mathbf{r}}$ and $\bar{\mathbf{s}}$, respectively. Moreover, the spacing between the isoparametric waves of the r^* field equals $\bar{\chi}\cos(\bar{\theta})$ if the interval of r^* value is equal to 1; similarly, the spacing between the isoparametric waves of the s^* field is $\cos(\bar{\theta})$. Therefore, the segment lengths along $\bar{\mathbf{r}}$ and $\bar{\mathbf{s}}$ directions are 1 and $\bar{\chi}$, respectively. Consequently, the (approximated) parallelograms formed by two groups of intersecting isoparametric waves conform to the optimized transformation variables ($\bar{\chi}$, $\bar{\theta}$, and $\bar{\varphi}$), and all these isoparametric waves visually construct the desired mesh.

4.4.2. Mesh extraction from isoparametric waves

To extract the transformation-guided mesh from the isoparametric waves, we leverage computer vision techniques as follows. As shown in Fig. 7(a), we treat the isoparametric waves as an image (a third-order tensor). We then apply the convolution operation to detect the inner and outer boundaries of isoparametric waves (Fig. 7(b)), which have finite widths in an image. Next, we identify the inner boundaries and approximate them as quadrilaterals with the Douglas–Peucker algorithm (Visvalingam and Whyatt, 1990) (Fig. 7(c)). Finally, we merge the nearby points into one to form a fully connected mesh (Fig. 7(d)) and reorder the element vertices to conform to the optimized transformation variables.

We highlight that this mesh extraction technique applies to various complex patterns. Fig. 7(e) demonstrates mesh extraction from general hand-drawn patterns, showcasing the technique's resilience in handling low-quality, disconnected, and singular patterns. Leveraging this mesh extraction technique enables the creation of an unstructured mesh that adheres to the optimized transformation variables ($\bar{\chi}$, $\bar{\theta}$, and $\bar{\varphi}$). Finally, we can use the unstructured virtual growth algorithm in Section 2 to grow building blocks within this transformation-guided unstructured mesh and create optimized transformed metastructures.

5. Numerical examples

In this section, we present three sets of numerical examples to illustrate optimized transformed metastructures discovered by proposed frequency- and transformation-based topology optimization, where we also reveal underlying mechanisms that drive the optimized mechanical responses. First, we present metastructures engineered for maximized global stiffness in Section 5.1. Here, we compare the stiffness of both untransformed and transformed metastructures, highlighting the stiffness augmentation enabled by microstructural transformation through expanded material property space. We also perform a convergence study to demonstrate the consistency between microscale and macroscale stiffness. Subsequently, we discover metastructures with unidirectional mechanical cloaking functionalities in Section 5.2. Here, we focus on how building block selection and the manipulation of their frequency combination affect the cloaking effect. Finally, Section 5.3 demonstrates the utility of the discovered metastructures as mechanical infills with target local stiffness.

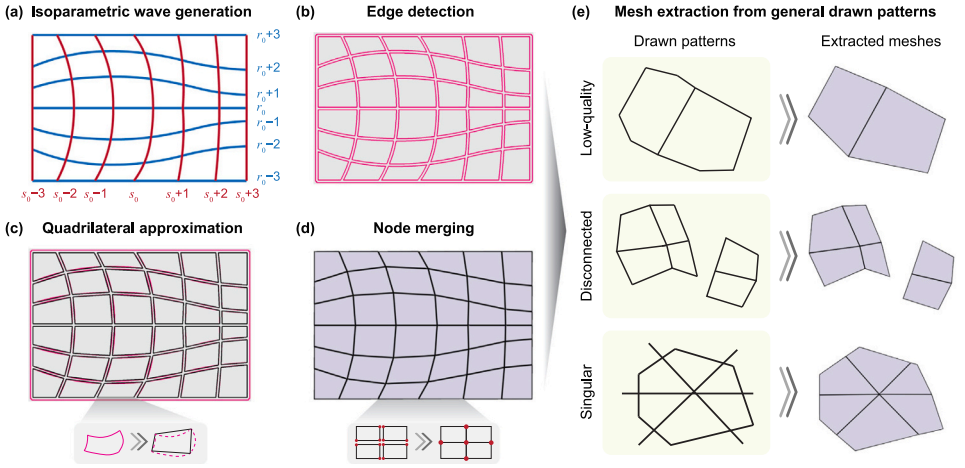

Fig. 7. Mesh extraction from isoparametric waves. (a) Isoparametric waves generated based on global parameterization. The dummy integers, r_0-3–r_0+3 and s_0-3–s_0+3, represent the isoparametric waves. (b) Edges (contours) detected by the convolution operation. (c) Quadrilaterals approximated based on internal contours. (d) Derived mesh after merging nearby nodes. (e) Mesh extraction from general hand-drawn patterns.

To discover metastructures in these examples, we implement proposed frequency- and transformation-based topology optimization in Section 4 by leveraging the open-source FEniTop (Jia et al., 2024c) (FEniCSx-based (Baratta et al., 2023) topology optimization supporting parallel computing), PyTorch (Ketkar et al., 2021) (for machine learning), and OpenCV (Bradski, 2000) (for computer vision) software. When generating the training data for the neural network and performing topology optimization, we constrain the physical transformation variables within the subsets of feasible ranges. Specifically, we adopt $\overline{\chi} \in [\chi^{\mathrm{l}}, \chi^{\mathrm{u}}] = [1/3, 3] \subset (0, +\infty)$ for the relative scaling, $\overline{\theta} \in [\theta^{\mathrm{l}}, \theta^{\mathrm{u}}] = [-\pi/4, \pi/4] \subset (-\pi/2, \pi/2)$ for the skew angle, and $\overline{\varphi} \in [\varphi^{\mathrm{l}}, \varphi^{\mathrm{u}}] = [-\pi/3, \pi/3] \subset [-\pi/2, \pi/2]$ for the rotation angle. These subsets ensure coverage of a broad spectrum of achievable material properties based on Fig. 4. In addition, using these subsets requires less training data in Section 3.3 and promotes the solution existence during transformation-guided mesh generation in Section 4.4. For all examples in this study, we focus on 2D problems for simplicity and adopt the plane stress assumption.

5.1. Global stiffness maximization

We begin by discovering metastructures with maximized global stiffness (i.e., the objective in (9)). Fig. 8(a) shows the design setup including the design domain, boundary conditions, design variables, and optimization objective. The design domain is a square with the left edge partially fixed, and we apply downward displacement loading with an amplitude of $\overline{u} = 1$ mm on the middle part of the right edge. In this example, we simultaneously optimize the macroscale density (microstructural existence), frequency (building blocks' frequency combination), and transformation (microstructural relative scaling, skew, and rotation) variables. The objective is to maximize the global stiffness of the metastructure (K), which is quantified as the slope of the force (F) –displacement (u) curve and can be computed as

$$K = \frac{1}{\overline{u}^2} \int_{\Omega} \mathbf{E} : \mathbb{C} : \mathbf{E} \mathrm{d}\mathbf{X}.$$

To proceed with topology optimization, we discretize the design domain with a structured mesh consisting of 40,000 bilinear quadrilateral macroscale elements. The remaining topology optimization parameters are as follows. The maximum optimization iteration is 200. The allowable volume fraction is $\overline{V} = 0.3$. The filter radius is $R = 2$ mm for all design variables. The Heaviside sharpness parameter is $\beta = 1$ initially and doubled every 30 optimization iterations until $\beta = 128$. The bound of the frequency variable is $[0, 1]$. The move limit in the MMA optimizer is $m = 0.05$.

Upon finishing topology optimization, we derive the optimized transformed metastructure in Fig. 8(b), where we also present the optimized untransformed metastructure as a reference. For both metastructures, Fig. 8(b) presents their optimized macroscale design variables, including density, frequency, and transformation fields. The top row in Fig. 8(b) illustrates the macroscale density and frequency variables, where the colored part signifies microstructural existence. Further, blue and red colors imply that the microstructure is dominated by `cross` and `ring` building blocks, respectively. The middle row in Fig. 8(b) shows the macroscale transformation variables expressed with the cross-field defined in Fig. 3.

In Fig. 8(b), while the untransformed metastructure freezes microstructural transformation, this metastructure still optimally places the building blocks — putting `cross` building blocks within the horizontal members on the top and bottom and `ring` building blocks within the inclined members in the middle — such that building blocks' members align with the macroscale topology, and the latter further follows the load paths of the structure. In addition to optimally placing the building blocks, the transformed metastructure also enables load-path-oriented microstructural transformation and improves structural stiffness by 35.8% from 7.70 to

Table 1
Statistics of the convergence study for the untransformed metastructure in Fig. 8(d) (unit of stiffness: N/mm).

k values	Cell numbers	DOF numbers	Ave. stiffness	Std. of stiffness	Stiffness errors
1	6,743	27,751,804	6.8555	0.0124	−10.97%
2	27,085	29,187,266	7.0045	0.0016	−9.03%
3	60,976	25,880,187	7.1944	0.0110	−6.57%
4	108,270	29,601,318	7.4417	0.0020	−3.35%
5	169,041	26,190,513	7.6975	0.0034	−0.03%

Table 2
Statistics of the convergence study for the transformed metastructure in Fig. 8(d) (unit of stiffness: N/mm).

k values	Cell numbers	DOF numbers	Ave. stiffness	Std. of stiffness	Stiffness errors
1	6,600	31,115,372	8.8899	0.0011	−15.01%
2	26,416	32,578,211	9.2836	0.0024	−11.25%
3	59,402	29,864,827	9.4426	0.0015	−9.73%
4	105,626	33,176,502	9.7594	0.0010	−6.70%
5	164,966	30,945,209	9.9759	0.0011	−4.63%

10.46 N/mm. The bottom row in Fig. 8(b) illustrates both metastructures at the microscale, and we observe the seamless integration between neighboring building blocks despite the microstructural transformation.

To understand the stiffness improvement enabled by optimizing microstructural transformation, we plot the material property space for both untransformed and transformed metastructures in Fig. 8(c). Here, x-axis is the normalized average Young's modulus defined as (Liu et al., 2022)

$$\overline{E}_{\text{ave}} = \frac{1}{2E_0}\left(\frac{1}{\mathbb{S}_{1111}} + \frac{1}{\mathbb{S}_{2222}}\right)$$

and y-axis is the average Poisson's ratio given as (Liu et al., 2022)

$$\nu_{\text{ave}} = -\frac{1}{2}\left(\frac{\mathbb{S}_{2211}}{\mathbb{S}_{1111}} + \frac{\mathbb{S}_{1122}}{\mathbb{S}_{2222}}\right).$$

The variable E_0 is the Young's modulus of the isotropic base material forming the building blocks, and $\mathbb{S}$ is the homogenized compliance tensor. In Fig. 8(c), the material property space is spanned by the discrete material properties in Section 3, and the data points plotted here represent the properties used in the optimized metastructures in Fig. 8(b). Based on Fig. 8(c), the untransformed material property space is collapsed into a straight line, while the transformed space features an expanded region. Moreover, most of the material data used in the transformed metastructure falls outside the straight line (untransformed material property space), demonstrating the necessity of incorporating microstructural transformation to improve structural stiffness.

Despite the promising stiffness improvement at the macroscale (Fig. 8(b)), it is crucial to examine the consistency and reproducibility of the performance gain at the microscale. Following Jia et al. (2024a,b), we perform a convergence study for both untransformed and transformed metastructures as follows. We begin by generating transformation-guided meshes with a uniform macroscale element size of $h = 0.33$ mm. Each macroscale element is subsequently partitioned into k^2 cells (Fig. 2), where k represents the number of cells in one direction within each macroscale element. Next, we grow building blocks within those cells and yield both untransformed and transformed metastructures with different resolutions. In this procedure, we explore values of k ranging from 1 to 5 for both metastructures and generate 5 samples for each k value (recall the virtual growth algorithm is stochastic). Finally, we perform standard FEA on these metastructures at the microscale and evaluate their stiffness.

Fig. 8(d) shows the convergence study of both untransformed and transformed metastructures, and Tables 1–2 further provide detailed statistics including k values, cell numbers, DOF numbers, average (ave.) stiffness, sample standard deviations (std.) of stiffness, and the relative errors between the microscale and macroscale stiffness. The observations are as follows. First, for an identical macroscale design with the same k value, all five sample microscale metastructures exhibit similar stiffness. This similarity of stiffness manifests as the negligible sample standard deviation, suggesting a high reproducibility of mechanical performance despite the stochastic nature of the microscale metastructures. Second, as the k value increases, the microscale stiffness of both untransformed and transformed metastructures converges to the corresponding macroscale values. This convergence results from the imposition of a stronger contrast of the length scales between the microstructure and metastructure.

To conclude, optimizing transformation can enhance structural stiffness thanks to the expanded material property space (see Appendix F for further comparisons with periodic designs). This mechanical performance improvement is consistent between different scales and reproducible at the microscale based on the convergence study in Fig. 8(d) and Tables 1–2. We note that, while both untransformed and transformed metastructures exhibit negligible stiffness errors (less than 5%) when $k = 5$, the transformed design shows a slightly higher discrepancy. This variance could potentially be mitigated by enlarging the training dataset or exploring more precise methods for mesh extraction.

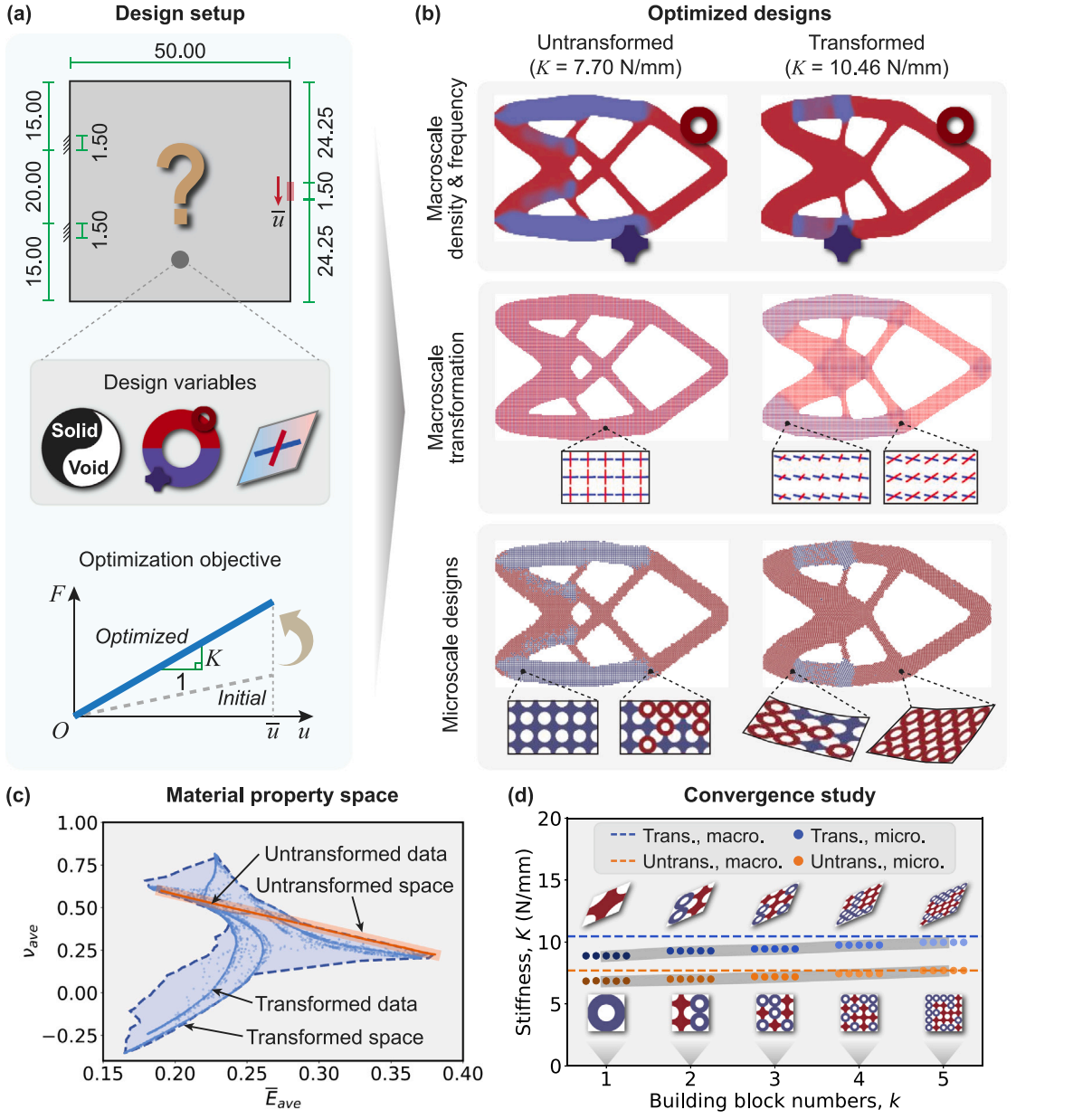

Fig. 8. Discovering metastructures with maximized global stiffness. (a) Design setup including the design domain, boundary conditions, design variables, and optimization objective. The variable $\bar{u}$ is the amplitude of the applied displacement. (b) Optimized untransformed and transformed metastructures. (c) Comparison of the untransformed and transformed material property spaces. The material property space is spanned by the discrete data in Section 3, and the data points plotted here correspond to the properties used in the optimized metastructures in (b). (d) Convergence study of the global stiffness (K) with increasing building block numbers (k). The dashed lines are the macroscale stiffness, and the dots are the microscale ones of sample metastructures. The shaded lines show the trend of the microscale stiffness with increasing building block numbers. The insets illustrate the microstructures with and without transformation.

5.2. Unidirectional mechanical cloaking

In this section, we control another important type of structural response — displacement field — to achieve unidirectional mechanical cloaking (*i.e.*, the objective in (10)). In this example, we also investigate how building block selection and the manipulation of their frequency combination influence the cloaking effect. In Fig. 9(a), we examine a square reference structure subjected to two load cases with the same applied displacement amplitude, $\bar{u}$ = 1 mm. Under these load conditions, both x- and y-displacements exhibit relative uniformity across the structure. To conceal objects, we introduce five irregular holes and yield the

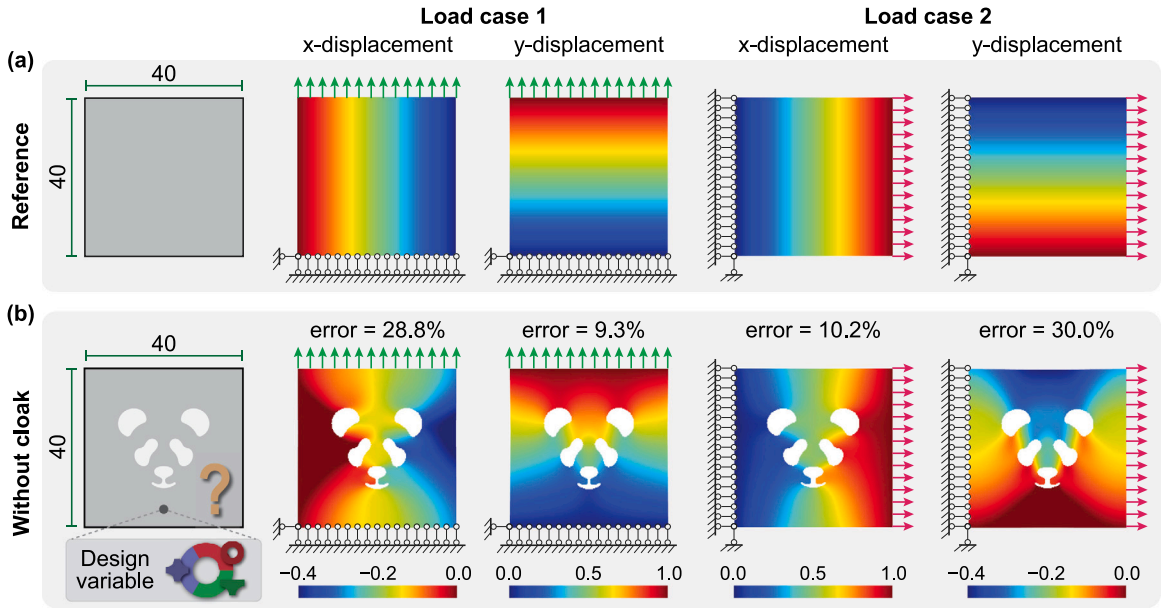

Fig. 9. Design setup of the Unidirectional mechanical cloaking example. (a) Reference structure with uniform x- and y-displacements under two load cases. (b) Uncloaked structure with distorted displacements. The design objective is to recover the distorted displacements to the uniform ones in (a) by optimizing the frequency combination of building blocks.

uncloaked structure in Fig. 9(b). Notably, the x- and y-displacements visibly deviate from their counterparts in Fig. 9(a), with relative errors ranging from 9.3% to 30.0%. Our goal is to restore the distorted displacements to the uniform state in Fig. 9(a) (known as unidirectional mechanical cloaking (Wang et al., 2022a)) by optimizing the frequency combination of building blocks.

To initiate the topology optimization process, we discretize the design domain using 40,000 bilinear quadrilateral macroscale elements. The remaining topology optimization parameters are as follows. The maximum optimization iteration is 400. The filter radius is $R = 1$ mm for the frequency variables. The bound of the frequency variable is $[0, 1]$. The move limit in the MMA optimizer is $m = 0.05$. To focus on the influence of building block selection on the cloaking effect, we freeze the density ($\overline{\rho} \equiv 1$) and transformation ($\overline{\chi} \equiv 1$, $\overline{\theta} \equiv 0$, and $\overline{\varphi} \equiv 0$) variables in this example.

Fig. 10(a) shows two optimized metastructures with different building block selections. Metastructure 1 employs `cross` and coupled `letter T` building blocks while metastructure 2 incorporates `ring`, `cross`, and uncoupled `letter T` building blocks. Here, a coupled building block represents that all building block variations (Fig. 2(a)) equally inherit the frequency of the primitive building block. For example, given a coupled `letter T` building block with a desired frequency denoted as $\overline{\xi}_{\mathrm{T}}$, the frequencies of its four variations are coupled as $\overline{\xi}_{\mathrm{T},1} = \overline{\xi}_{\mathrm{T},2} = \overline{\xi}_{\mathrm{T},3} = \overline{\xi}_{\mathrm{T},4} = \overline{\xi}_{\mathrm{T}}/4$. On the contrary, for an uncoupled `letter T` building block, we treat the frequencies of building block variations as independent variables subjected to $\overline{\xi}_{\mathrm{T},1} + \overline{\xi}_{\mathrm{T},2} + \overline{\xi}_{\mathrm{T},3} + \overline{\xi}_{\mathrm{T},4} = \overline{\xi}_{\mathrm{T}}$. This simple coupling/uncoupling treatment enables the metastructure to select less/more anisotropic microstructures, as demonstrated in the zoom-in views in Fig. 10(a).

To examine the cloaking effect of the two optimized metastructures in Fig. 10(a), we perform standard FEA to analyze their x- and y-displacements under the two load cases at both macroscale and microscale. Fig. 10(b) displays the displacements of metastructure 1. Comparing these results with Fig. 9(b), we observe a reduction in displacement errors from 9.3%–30.0% to 7.2%–26.4% at the macroscale and 8.2%–26.0% at the microscale. Despite the reduction in displacement error, the cloaking effect remains relatively poor due to a conservative building block selection.

Next, we assess the displacements of metastructure 2 at both the macroscale and microscale, as shown in Fig. 10(c). Upon close examination, we observe an apparent displacement error reduction compared to Fig. 10(b) — reducing from 7.2%–26.4% to 2.1%–5.6% at the macroscale and from 8.2%–26.0% to 3.6%–10.8% at the microscale. This effective error reduction is achieved simply by uncoupling the `letter T` building block and incorporating the `ring` building block.

To understand how building block selection affects the mechanical cloaking effect, we compare the optimized material properties between metastructures 1 and 2, as shown in Fig. 11. In Fig. 11(a), metastructure 1 features a discrete material property distribution, taking either minimum or maximum values, due to the limited choice of building blocks (`cross` and coupled `letter T`). In contrast, metastructure 2 leverages continuous material properties enabled by the free selection among multiple building blocks (`ring`, `cross`, and uncoupled `letter T`). In Fig. 11(b), we closely examine the distribution of optimized material properties and observe that the building block selection of metastructure 2 provides not only continuous material properties but also a wider range of them. We emphasize that both factors contribute to fitting-type objectives (Wang et al., 2022a; Jia et al., 2024a). Consequently, metastructure 2 demonstrates superior mechanical cloaking performance.

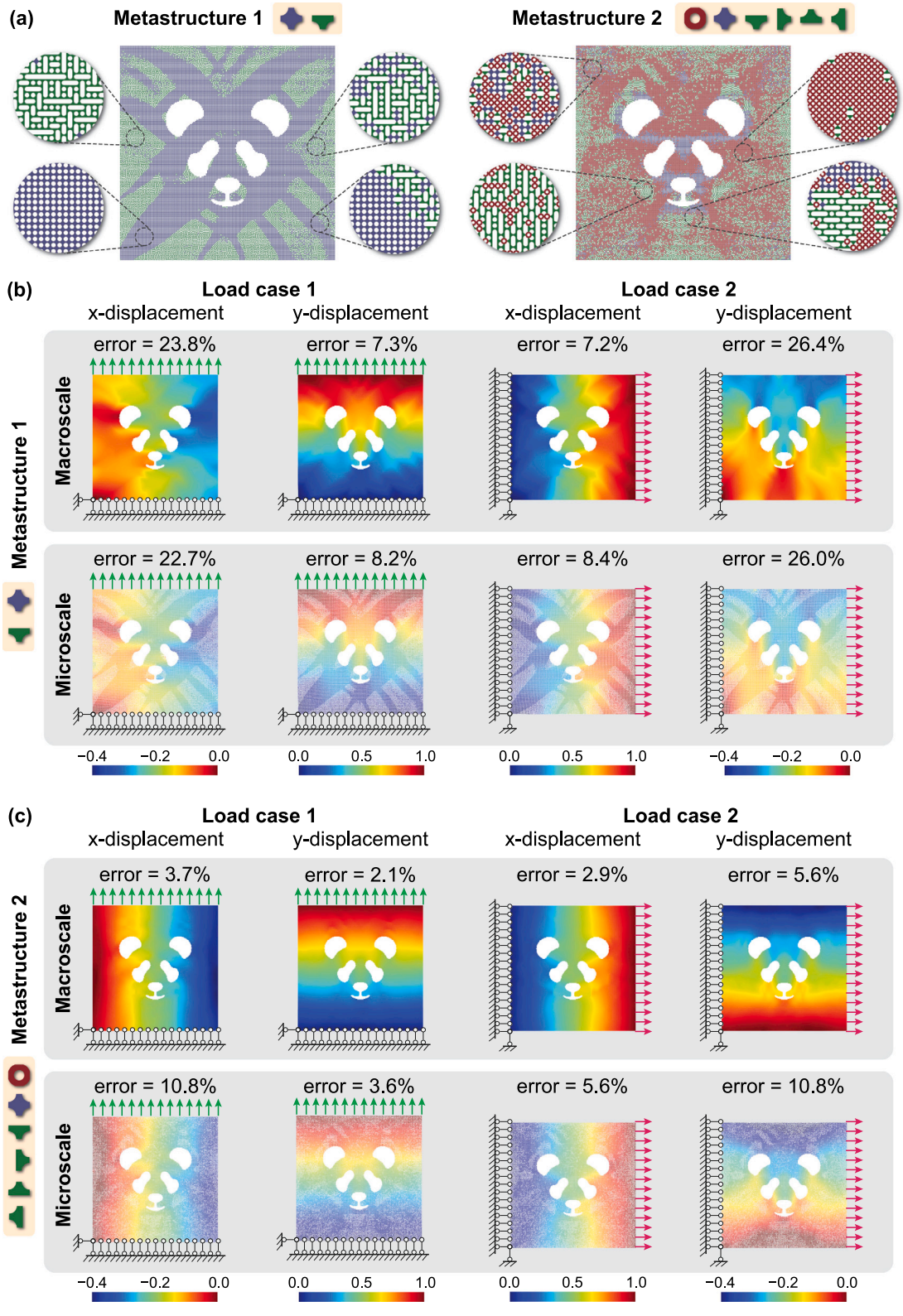

Fig. 10. Comparison of optimized metastructures stemming from different building block selections. (a) Two optimized metastructures with different building blocks. Metastructure 1 uses `cross` and coupled `letter T` building blocks; metastructure 2 uses `ring`, `cross`, and uncoupled `letter T` building blocks. The insets show diverse microstructures generated from different building blocks. (b) The macroscale and microscale displacements of metastructure 1 under two load cases. (c) The corresponding displacements of metastructure 2.

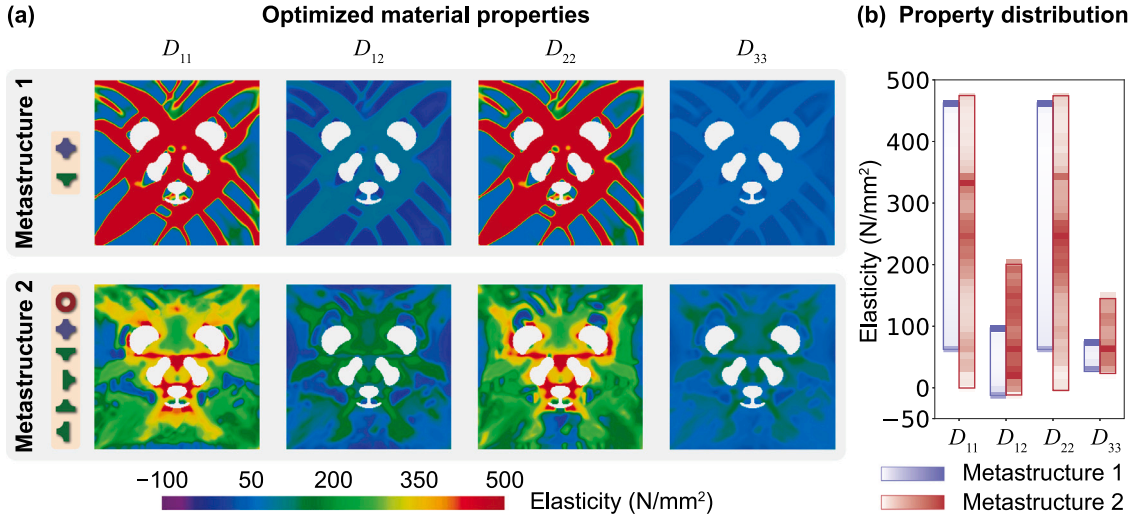

Fig. 11. Comparison of optimized material properties between metastructures 1 and 2 in Fig. 10(a). (a) Optimized material properties. The variables D_{11}, D_{12}, D_{22}, and D_{33} are four components of the homogenized elasticity matrix. (b) Optimized material property distribution. Dark colors represent the clustering of material properties.

After observing that the superior cloaking performance of metastructure 2 results from its ability to achieve a wider range of material properties, we further analyze how these properties are influenced by building block selection. Specifically, we focus on the directional elasticity of microstructures, D_{11} and D_{33}, as shown in Fig. 12. Figs. 12(a)–(c) present D_{11} and D_{33} in a polar coordinate system for various building block selections. Here, the radial distance is the component value, and the angle represents the loading direction. Each component value is averaged over 30 samples with the same building block selection and frequency combination. In Fig. 12(a), we consider the uncoupled `letter T` building block and observe that uncoupling the frequencies of building block variations leads to increased anisotropy and higher elasticity compared to the coupled one (*i.e.*, the green curve). This increase is achieved by positioning more microstructural members toward the loading direction. By further introducing the `cross` building block with uncoupled `letter T` building block (Fig. 12(b)), we broaden the elasticity surface while maintaining anisotropy. This effect is potentially due to the fact that the microstructural members are subjected to more confinement — the `cross` building block imposes confinement on nearby microstructural members in all four directions, whereas the `letter T` building block imposes confinement in only three directions — therefore becoming less deformable. In Fig. 12(c), we also incorporate the `ring` building block while keeping the `letter T` building block coupled for simplicity. With a higher proportion of the `ring` building block, the amplitude of elasticity increases generally due to more confinement imposed on microstructural members. Additionally, the principal directions shift from 0°–180° and 90°–270° to 45°–225° and 135°–315°, which is aligned with the geometries of the `ring` building block.

In summary, compared to a coupled building block, the uncoupled version promotes greater anisotropy and higher elasticity. Moreover, incorporating additional building blocks such as `ring` can also increase the elasticity amplitude and shift the principal directions. Consequently, by simply uncoupling the frequencies of building block variations and introducing new building blocks, we can broaden the range of achievable material properties and control the mechanical response toward complex targets (Fig. 10(c)).

5.3. Mechanical infills with target local stiffness

In this final example, we showcase the application of the proposed topology optimization methodology in designing mechanical infills with locally minimized/maximized stiffness (the objective in (11)). As shown in Fig. 13(a), we consider a complex design domain with a fixed bottom and subjected to a gravity-like body force with an amplitude of $\bar{b} = 0.02$ N/mm^2. Our objective is to populate building blocks within the design domain, ensuring that the dashed region is soft and the remaining part is stiff. To achieve this goal, we optimize the distribution of all six building block types in Fig. 2(a), namely `ring`, `cross`, `letter T`, `letter X`, `irregular 1`, and `irregular 2`.

To proceed with topology optimization, we discretize the design domain with a coarse mesh consisting of 658 bilinear quadrilateral macroscale elements with a similar size. We highlight that a coarse mesh is sufficient because the macroscale elements can be further divided into multiple cells with various building blocks to achieve higher resolution and better performance. In this examople, each macroscale element is further subdivided into 4 cells (more number of cells can be considered if necessary) based on the shape functions (Fig. 2(b)) such that the nearby cells have closely matching geometries. Next, we precompute the transformation variables ($\overline{\chi}$, $\overline{\theta}$, and $\overline{\varphi}$) to align with cell geometries and fix the transformation and density ($\overline{\rho} \equiv 1$) variables during optimization. As for the frequency variables, we require $\xi_1 - \xi_{M^{\texttt{freq}}} \in [0.1, 0.9]$ to facilitate the solution existence in the unstructured virtual growth

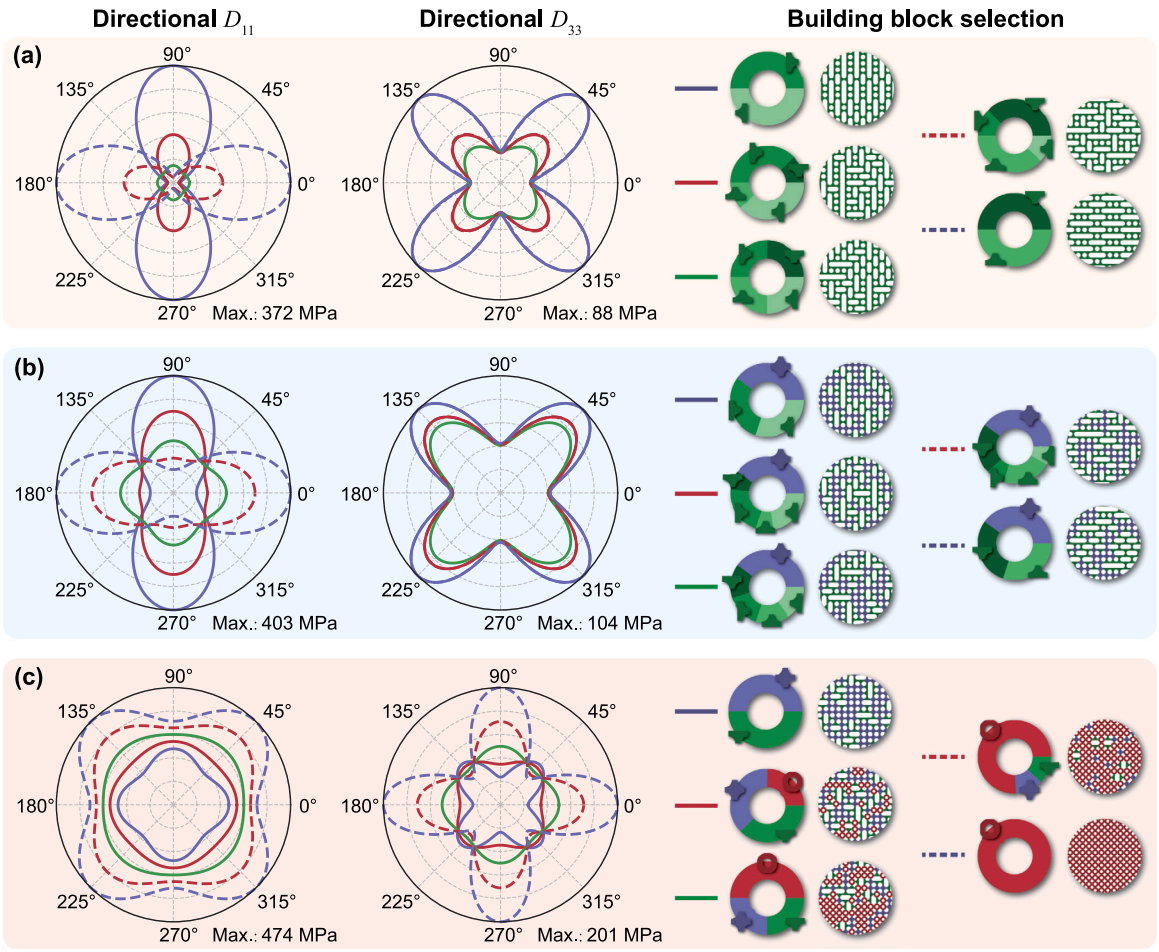

Fig. 12. Directional elasticity for various building block selections: (a) uncoupled `letter T` building block; (b) `cross` and uncoupled `letter T` building blocks; (c) `ring`, `cross`, and coupled `letter T` building blocks. D_{11} and D_{33} are two components of the homogenized elasticity matrix. The radial distance is the component value, and the angle represents the loading direction. All the "max." indicators denote the maximum directional elasticity. The green curve in (a) corresponds to the coupled `letter T` building block and is provided for reference.

algorithm in Section 2. The remaining topology optimization parameters are as follows. The maximum optimization iteration is 100. The filter radius is $R = 2$ mm for the frequency variables. The move limit in the MMA optimizer is $m = 0.05$.

Fig. 13(b) shows a reference metastructure featuring a uniform distribution of building blocks. The strain energy is $W_{\texttt{stiff}} = 24.47$ N·mm for the stiff part and $W_{\texttt{soft}} = 31.67$ N·mm for the soft part. Following topology optimization (Fig. 13(c)), the strain energy of the stiff part decreases to $W_{\texttt{stiff}} = 19.40$ N mm by 20.7%, representing a stiffness enhancement. As for the strain energy of the soft part, it increases to $W_{\texttt{soft}} = 60.48$ N mm by 91.0%, representing a stiffness reduction. Upon closer examination of the insets in Fig. 13(c), we observe that the stiff region prefers `ring` and `cross` building blocks, known for their higher directional elasticity (Fig. 12). On the contrary, the soft region prioritizes the remaining four building block types, especially for `letter` X. Through the optimal arrangement of building blocks, the proposed methodology identifies the suitable microstructures — including those reported in the literature such as Clausen et al. (2015) — to achieve the desired local stiffness.

In addition to achieving target local stiffness, the optimized metastructures can function as mechanical infills. It is because the derived metastructure guarantees to fit the given unstructured mesh (Fig. 2(c)), which in turn conforms to the design domain. While we acknowledge the great advances in designing mechanical infills such as Groen et al. (2021) and Jensen et al. (2024), the proposed approach further enables an explicitly controllable and globally uniform feature size provided that the finite element discretization of the design domain is sufficiently uniform. We also note that a uniform finite element discretization can be achieved with many commercial (such as Abaqus (Barbero, 2023)) and open-source (such as Gmsh (Geuzaine and Remacle, 2009)) software.

To demonstrate the effectiveness of the proposed method in designing mechanical infills, we examine various complex design domains in Fig. 13(d) and derive their corresponding optimized metastructures. Based on Fig. 13(d), all optimized transformed metastructures exhibit promising stiffness enhancement in the stiff region (exemplified by strain energy decreases ranging from 22.2% to 51.4%) and stiffness reduction in the soft region (exemplified by strain energy increases ranging from 63.2% to 111.4%). Notably, all optimized metastructures seamlessly conform to their respective design domains without the need for

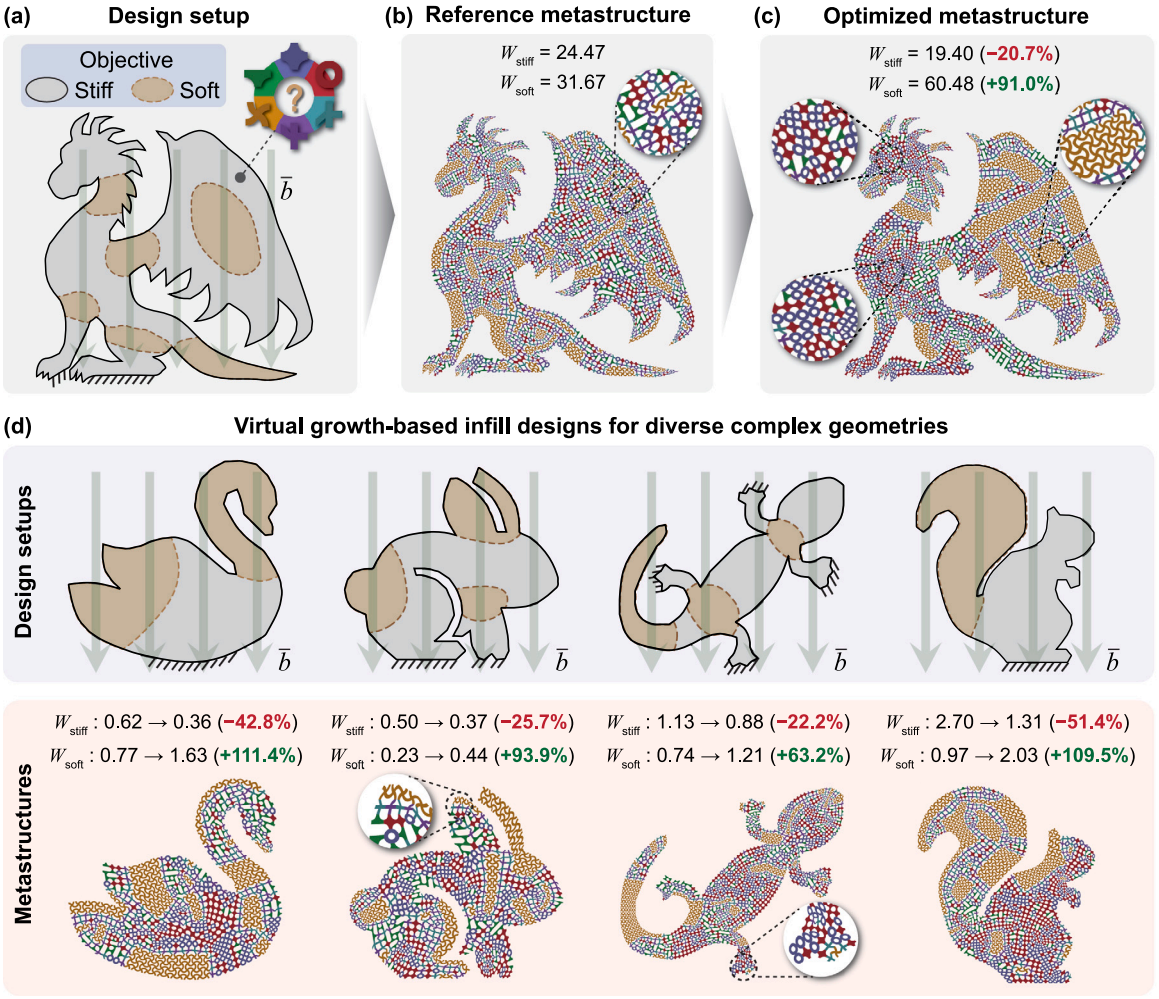

Fig. 13. Mechanical infills with target local stiffness. (a) Design setup including the design domain, boundary conditions, optimization objective, and design variable. The scalar $\bar{b}$ is the amplitude of the gravity-like body force. (b) Reference metastructure with a uniform distribution of building blocks. The variables W_{stiff} and W_{soft} (in N·mm) are the strain energies in the stiff and soft regions, respectively. (c) Optimized metastructure with spatially varying distribution of building blocks. The values in the parentheses are the energy decrease/increase compared to the reference structure. (d) Virtual growth-based infill designs for diverse complex geometries. The top row shows the design setups, and the bottom row displays the corresponding optimized transformed metastructures. The values before and after the arrow are the strain energies before and after optimization, respectively.

tedious post-processing. Furthermore, these metastructures display relatively uniform feature sizes, which are crucial for successful manufacturing (Jia et al., 2024a,b) due to the trade-off between the printing volume and resolution in many modern manufacturing techniques.

6. Conclusions

In this study, we introduce a design methodology aimed at discovering transformed metastructures with optimized mechanical responses, while also revealing the underlying mechanisms driving these responses. To establish this methodology, we begin by proposing an unstructured virtual growth algorithm, facilitating the seamless growth of building blocks on an unstructured mesh to generate metastructures with desired building block distribution. Next, we present frequency-controlled and transformed homogenized elasticity to establish the constitutive relationships between frequency and transformation variables, as well as the homogenized elasticity matrix of microstructures. Leveraging the unstructured virtual growth algorithm and the established constitutive relationships, we propose frequency- and transformation-based topology optimization to simultaneously optimize building block distribution and transformation, generating metastructures with optimized mechanical responses. Finally, we present three sets of numerical examples to demonstrate the effectiveness of the framework and study metastructures that achieve maximized global stiffness, unidirectional mechanical cloaking, and target local stiffness as mechanical infill.

Based on the presented numerical examples, the generated metastructures effectively obtain the desired mechanical responses, which are consistent between the microscale and macroscale. We highlight that these achieved responses result from the vast material property space enabled by different frequency combinations of building blocks as well as transformations of microstructures. Additionally, thanks to the unstructured virtual growth algorithm, the generated metastructures are made of microstructures seamlessly formed by building blocks with explicitly controllable feature sizes. Consequently, the created metastructures naturally fit complex design domains and function as mechanical infills suitable for manufacturing. Looking ahead, we anticipate that the presented design approach can be extended to 3D, necessitating a method that can effectively generate transformation-guided meshes in higher dimensions. Additionally, the proposed methodology can be further enhanced to reveal optimized transformed metastructures that couple mechanics with other physics, which is our ongoing work.

CRediT authorship contribution statement

Yingqi Jia: Writing – review & editing, Writing – original draft, Visualization, Software, Methodology, Investigation, Formal analysis, Data curation, Conceptualization. **Ke Liu:** Writing – review & editing, Writing – original draft, Methodology, Conceptualization. **Xiaojia Shelly Zhang:** Writing – review & editing, Writing – original draft, Supervision, Resources, Project administration, Methodology, Investigation, Funding acquisition, Conceptualization.

Declaration of competing interest

The authors declare that they have no known competing financial interests or personal relationships that could have appeared to influence the work reported in this paper.

Data availability

Data will be made available on request.

Acknowledgments

The authors would like to devote this paper to the Special Issue in honor of Professor Huajian Gao for his contributions to Mechanics of Materials and Structures on the occasion of his 60th birthday. Authors X.S.Z. and Y.J. acknowledge the support from the David C. Crawford Faculty Scholar Award from the Department of Civil and Environmental Engineering in the Grainger College of Engineering at the University of Illinois. The information provided in this paper is the sole opinion of the authors and does not necessarily reflect the view of the sponsoring agency.

Appendix A. Adjacency rules for the unstructured growth of metastructures

In this section, we introduce the adjacency rules for the unstructured growth of metastructures. As shown in Fig. A.14(a), we begin by converting building block variations to their corresponding binary representations (a pixelization process). A binary representation is an N-by-N matrix with all elements taking values in $\{0, 1\}$, where 0 represents a void and 1 represents a solid. For the building block variations considered in this study, it is sufficient to set $N = 7$.

Based on the binary representations, we can apply adjacency rules to determine if a pair of given building block variations can be adjacent (Fig. A.14(b)). Specifically, we define an adjacency indicator as

$$\mathcal{I} = \|\mathbf{R}^{\texttt{left}}_{*N} - \mathbf{R}^{\texttt{right}}_{*1}\|_2^2,$$

where $\mathbf{R}^{\texttt{left}}$ and $\mathbf{R}^{\texttt{right}}$ are the binary representations of the two building block variations on the left and right, respectively. The symbol $\mathbf{R}_{*m}$ represents the mth column of the matrix $\mathbf{R}$. Following Liu et al. (2022) and Jia et al. (2024b,a), the two building block variations can be adjacent if and only if their neighboring boundaries match each other ($\mathcal{I} = 0$).

Built upon the pairwise adjacency rules, we can identify the admissible building blocks for unfilled cells in the unstructured mesh. As shown in Fig. A.14(c), for an unfilled cell of interest, we apply the adjacency rules (Fig. A.14(b)) to all its neighbors and derive the building block variations that can be adjacent to them. By taking the intersection of the derived building block variations, we obtain the admissible building blocks for the current cell.

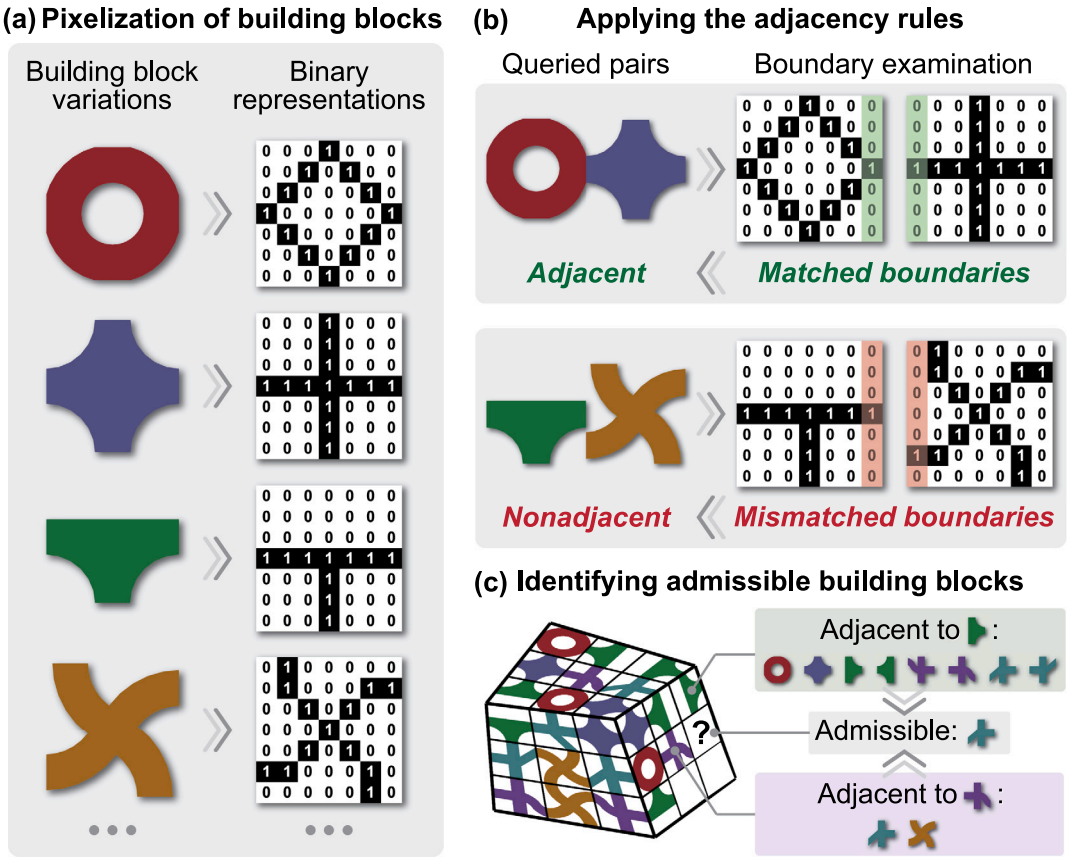

Fig. A.14. Adjacency rules for the unstructured growth of metastructures. (a) Pixelization of building blocks. (b) Applying the adjacency rules. (c) Identifying the admissible building blocks.

Appendix B. Numerical homogenization for the elasticity matrix

In this section, we briefly review the numerical homogenization theory in Vigliotti and Pasini (2012), which is used to evaluate the homogenized elasticity matrix in this work and serves as the basis to prove the invariance of homogenized elasticity under uniform scaling in Section 3.2. Without loss of generality, we consider a 3D unit cell (or a microstructure here) with periodic vectors, $\mathbf{a}_1$, $\mathbf{a}_2$, and $\mathbf{a}_3$. We discretize this microstructure with finite elements and identify the independent and dependent DOFs. We then figure out the topological matrices, $\mathbf{B}_0$ and $\mathbf{B}_a$, such that

$$\mathbf{d} = \mathbf{B}_0\mathbf{d}_0 + \mathbf{B}_a\Delta\mathbf{a} \tag{B.1}$$

where $\mathbf{d}$ and $\mathbf{d}_0$ are the displacement vectors of all DOFs and independent DOFs, respectively. The variable $\Delta\mathbf{a} = [\Delta\mathbf{a}_1^\top, \Delta\mathbf{a}_2^\top, \Delta\mathbf{a}_3^\top]^\top$ consists of the changes in periodic vectors due to deformation, $\Delta\mathbf{a}_1$, $\Delta\mathbf{a}_2$, and $\Delta\mathbf{a}_3$. Note that (B.1) represents the periodic boundary condition, and it implies a separation of length scales between the microstructure and the entire metastructure.

Based on FEA, we evaluate the global stiffness matrix of the discretized microstructure as $\mathbf{K}_\mathrm{m}$ and establish the periodic equilibrium equation as

$$\mathbf{B}_0^\top\mathbf{K}_\mathrm{m}\mathbf{d} = \mathbf{0}. \tag{B.2}$$

Substituting (B.1) into (B.2) yields

$$\mathbf{B}_0^\top\mathbf{K}_\mathrm{m}(\mathbf{B}_0\mathbf{d}_0 + \mathbf{B}_a\Delta\mathbf{a}) = \mathbf{0} \Rightarrow \mathbf{B}_0^\top\mathbf{K}_\mathrm{m}\mathbf{B}_0\mathbf{d}_0 = -\mathbf{B}_0^\top\mathbf{K}_\mathrm{m}\mathbf{B}_a\Delta\mathbf{a},$$

and we obtain the displacement vector of independent DOFs as

$$\mathbf{d}_0 = -(\mathbf{B}_0^\top\mathbf{K}_\mathrm{m}\mathbf{B}_0)^+\mathbf{B}_0^\top\mathbf{K}_\mathrm{m}\mathbf{B}_a\Delta\mathbf{a} := \mathbf{D}_0\Delta\mathbf{a}. \tag{B.3}$$

Substituting (B.3) into (B.1) gives the displacement vector of all DOFs as

$$\mathbf{d} = (\mathbf{B}_0\mathbf{D}_0 + \mathbf{B}_a)\Delta\mathbf{a} := \mathbf{D}_a\Delta\mathbf{a}.$$

We then evaluate the microscopic strain energy as

$$W_{\mathtt{micro}} = \frac{1}{2}\mathbf{d}^\top\mathbf{K}_{\mathtt{m}}\mathbf{d} = \frac{1}{2}\Delta\mathbf{a}^\top\mathbf{D}_a^\top\mathbf{K}_{\mathtt{m}}\mathbf{D}_a\Delta\mathbf{a} := \frac{1}{2}\Delta\mathbf{a}^\top\mathbf{K}_{\Delta\mathbf{a}}\Delta\mathbf{a}.$$

We now apply a dummy macroscopic strain field of $\boldsymbol{\epsilon}_{\mathtt{macro}}$ on the microstructure. According to the definition of the infinitesimal strain, we have $\Delta\mathbf{a}_i = \boldsymbol{\epsilon}_{\mathtt{macro}}\mathbf{a}_i$ for $i = 1, 2, 3$. We can then find a matrix, $\mathbf{B}_\epsilon$, such that $\Delta\mathbf{a} = \mathbf{B}_\epsilon\boldsymbol{\epsilon}^{\mathtt{V}}_{\mathtt{macro}}$ where $\boldsymbol{\epsilon}^{\mathtt{V}}_{\mathtt{macro}}$ is the Voigt notation of $\boldsymbol{\epsilon}_{\mathtt{macro}}$. Next, we can rewrite the microscopic strain energy as

$$W_{\mathtt{micro}} = \frac{1}{2}(\boldsymbol{\epsilon}^{\mathtt{V}}_{\mathtt{macro}})^\top\mathbf{B}_\epsilon^\top\mathbf{K}_{\Delta\mathbf{a}}\mathbf{B}_\epsilon\boldsymbol{\epsilon}^{\mathtt{V}}_{\mathtt{macro}}.$$

Based on continuum mechanics (Hughes, 2012), the macroscopic strain energy is expressed as

$$W_{\mathtt{macro}} = \frac{1}{2}(\boldsymbol{\epsilon}^{\mathtt{V}}_{\mathtt{macro}})^\top\mathbf{D}_{\mathtt{H}}\boldsymbol{\epsilon}^{\mathtt{V}}_{\mathtt{macro}}V$$

where $\mathbf{D}_{\mathtt{H}}$ is the homogenized elasticity matrix to be determined, and $V = \det([\mathbf{a}_1, \mathbf{a}_2, \mathbf{a}_3])$ is the microstructural volume. By equating the energy between the microscale and macroscale (*i.e.*, $W_{\mathtt{micro}} = W_{\mathtt{macro}}$), we derive

$$\mathbf{D}_{\mathtt{H}} = \frac{1}{V}\mathbf{B}_\epsilon^\top\mathbf{K}_{\Delta\mathbf{a}}\mathbf{B}_\epsilon.$$

Here, recall $\mathbf{K}_{\Delta\mathbf{a}} = \mathbf{D}_a^\top\mathbf{K}_{\mathtt{m}}\mathbf{D}_a$, $\mathbf{D}_a = \mathbf{B}_0\mathbf{D}_0 + \mathbf{B}_a$, and $\mathbf{D}_0 = -(\mathbf{B}_0^\top\mathbf{K}_{\mathtt{m}}\mathbf{B}_0)^+\mathbf{B}_0^\top\mathbf{K}_{\mathtt{m}}\mathbf{B}_a$, where $\mathbf{B}_0$, $\mathbf{B}_a$, $\mathbf{B}_\epsilon$, $\mathbf{K}_{\mathtt{m}}$, and V are ready to compute for a given microstructure.

We remark that this homogenization method requires the periodicity of the microstructure (unit cell), and it predicts the homogenized material properties by imposing periodic boundary conditions on the unit cells and ensuring energy conservation between the two scales. During this process, we only need to compute the stiffness matrix of the unit cell ($\mathbf{K}_{\mathtt{m}}$) instead of that of the entire design domain, which can be done with relatively low computational cost. Additionally, we highlight that this homogenization method is applicable to transformed microstructures by aligning the periodic vectors ($\mathbf{a}_1$, $\mathbf{a}_2$, and $\mathbf{a}_3$) with the transformed geometries.

Appendix C. Global stiffness matrix of a microstructure under uniform scaling

In this section, we derive the global stiffness matrix of a microstructure under uniform scaling. We begin by briefly reviewing the evaluation of the global stiffness matrix (Hughes, 2012) in the 2D case. Given shape functions, $N_1(\eta_1, \eta_2)$ and $N_2(\eta_1, \eta_2)$, we can express the global coordinates (X_1, X_2) as

$$X_1(\eta_1, \eta_2) = \sum_{i=1}^{N_e^{\mathtt{node}}} N_i(\eta_1, \eta_2)V_{e,i}^{[1]} \quad \text{and} \quad X_2(\eta_1, \eta_2) = \sum_{i=1}^{N_e^{\mathtt{node}}} N_i(\eta_1, \eta_2)V_{e,i}^{[2]}.$$

Here, (η_1, η_2) are the natural coordinates defined in $\Omega^\eta = [-1, 1] \times [-1, 1]$. The parameters $V_{e,i}^{[1]}$ and $V_{e,i}^{[2]}$ are X_1 and X_2 coordinates of ith node of finite element e in the microstructure, respectively. The parameter $N_e^{\mathtt{node}}$ is the number of nodes in finite element e. We can then compute the derivatives of shape functions as

$$\frac{\partial N_i}{\partial X_1} = \frac{1}{\mathcal{J}}\left(\frac{\partial N_i}{\partial \eta_1}\frac{\partial X_2}{\partial \eta_2} - \frac{\partial N_i}{\partial \eta_2}\frac{\partial X_2}{\partial \eta_1}\right) \quad \text{and} \quad \frac{\partial N_i}{\partial X_2} = \frac{1}{\mathcal{J}}\left(-\frac{\partial N_i}{\partial \eta_1}\frac{\partial X_1}{\partial \eta_2} + \frac{\partial N_i}{\partial \eta_2}\frac{\partial X_1}{\partial \eta_1}\right)$$

where $\mathcal{J}$ is the Jacobian determinant and expressed as

$$\mathcal{J} = \frac{\partial X_1}{\partial \eta_1}\frac{\partial X_2}{\partial \eta_2} - \frac{\partial X_1}{\partial \eta_2}\frac{\partial X_2}{\partial \eta_1}.$$

Based on the derivatives of shape functions, the global stiffness matrix of a microstructure can be expressed as (Hughes, 2012)

$$\mathbf{K}_{\mathtt{m}} = \mathop{\mathcal{A}}_{e=1}^{N^{\mathtt{elem}}} \int_{\Omega^\eta} \mathcal{J}\mathbf{B}_e^\top\mathbf{D}\mathbf{B}_e \mathrm{d}\Omega^\eta.$$

Here, $N^{\mathtt{elem}}$ is the number of microscale elements. $\mathbf{B}_e$ is the strain–displacement matrix of finite element e and consists of derivatives of shape functions, $\partial N_i/\partial X_1$ and $\partial N_i/\partial X_2$. The variable $\mathbf{D}$ is the elasticity matrix. The operator $\mathcal{A}$ represents the assembly of local stiffness matrices toward the global one.

We now uniformly scale the microstructure with a parameter s through the transformation rule, $\mathbf{x} = s\mathbf{X}$. The variables $\mathbf{X} \in \mathbb{R}^2$ and $\mathbf{x} \in \mathbb{R}^2$ represent the material points before and after transformation, respectively. This rule yields the transformed element nodes as $V_{e,i}^{\prime[1]} = sV_{e,i}^{[1]}$ and $V_{e,i}^{\prime[2]} = sV_{e,i}^{[2]}$. Consequently, we can derive the related transformed quantities as

$$\frac{\partial X_i'}{\partial \eta_j} = s\frac{\partial X_i}{\partial \eta_j}, \quad \mathcal{J}' = s^2\mathcal{J}, \quad \frac{\partial N_i}{\partial X_j'} = \frac{1}{s}\frac{\partial N_i}{\partial X_j}, \quad \text{and} \quad \mathbf{B}_e' = \frac{1}{s}\mathbf{B}_e.$$

Finally, the global stiffness matrix of the microstructure remains unchanged in 2D because

$$\mathbf{K}'_{\mathrm{m}} = \mathop{\mathcal{A}}_{e=1}^{N^{\mathrm{elem}}} \int_{\Omega^\eta} \mathcal{J}' \mathbf{B}'^{\top}_e \mathbf{D} \mathbf{B}'_e \mathrm{d}\Omega^\eta = \mathop{\mathcal{A}}_{e=1}^{N^{\mathrm{elem}}} \int_{\Omega^\eta} (s^2\mathcal{J}) \left(\frac{1}{s}\mathbf{B}_e\right)^{\top} \mathbf{D} \left(\frac{1}{s}\mathbf{B}_e\right) \mathrm{d}\Omega^\eta = \mathbf{K}_{\mathrm{m}}.$$

Similarly, we can derive the transformed global stiffness matrix in 3D as

$$\mathbf{K}''_{\mathrm{m}} = \mathop{\mathcal{A}}_{e=1}^{N^{\mathrm{elem}}} \int_{\Omega^\eta} (s^3\mathcal{J}) \left(\frac{1}{s}\mathbf{B}_e\right)^{\top} \mathbf{D} \left(\frac{1}{s}\mathbf{B}_e\right) \mathrm{d}\Omega^\eta = s\mathbf{K}_{\mathrm{m}},$$

which is scaled by a factor of s compared to the untransformed one ($\mathbf{K}_{\mathrm{m}}$).

Appendix D. Microstructural elasticity determined by rotation

In this section, we derive the microstructural elasticity matrix after rotation. Based on the linear transformation rule, rotating a microstructure counterclockwise (or rotating the axes clockwise) by angle $\overline{\varphi}$ can be expressed as

$$\mathbf{e}' = \mathbf{Q}\mathbf{e} \quad \Longleftrightarrow \quad \begin{bmatrix} \mathbf{e}'_1 \\ \mathbf{e}'_2 \end{bmatrix} = \begin{bmatrix} \cos\overline{\varphi} & -\sin\overline{\varphi} \\ \sin\overline{\varphi} & \cos\overline{\varphi} \end{bmatrix} \begin{bmatrix} \mathbf{e}_1 \\ \mathbf{e}_2 \end{bmatrix}$$

where both $\{\mathbf{e}_1, \mathbf{e}_2\}$ and $\{\mathbf{e}'_1, \mathbf{e}'_2\}$ form orthonormal bases, respectively. We then derive the rotated stress tensor ($\boldsymbol{\sigma}'$) as

$$\boldsymbol{\sigma} = \sigma'_{ij}\mathbf{e}'_i \otimes \mathbf{e}'_j = \sigma'_{ij}(Q_{im}\mathbf{e}_m) \otimes (Q_{jn}\mathbf{e}_n) = Q^{\top}_{mi}\sigma'_{ij}Q_{jn}\mathbf{e}_m \otimes \mathbf{e}_n = \mathbf{Q}^{\top}\boldsymbol{\sigma}'\mathbf{Q} \quad \Rightarrow \quad \boldsymbol{\sigma}' = \mathbf{Q}^{-\top}\boldsymbol{\sigma}\mathbf{Q}^{-1}$$

where $\boldsymbol{\sigma}$ is the stress tensor before rotation. Similarly, we express the rotated strain tensor ($\boldsymbol{\varepsilon}'$) as

$$\boldsymbol{\varepsilon}' = \mathbf{Q}^{-\top}\boldsymbol{\varepsilon}\mathbf{Q}^{-1},$$

and $\boldsymbol{\varepsilon}$ is the strain tensor before rotation.

For convenience, we express the stress ($\boldsymbol{\sigma}^{\mathrm{v}}$) and strain ($\boldsymbol{\varepsilon}^{\mathrm{v}}$) tensors in Voigt notations as

$$\boldsymbol{\sigma}^{\mathrm{v}} = \begin{bmatrix} \sigma_{11} \\ \sigma_{22} \\ \sigma_{12} \end{bmatrix} \quad \text{and} \quad \boldsymbol{\varepsilon}^{\mathrm{v}} = \begin{bmatrix} \varepsilon_{11} \\ \varepsilon_{22} \\ 2\varepsilon_{12} \end{bmatrix}$$

and then derive the rotated stress ($\boldsymbol{\sigma}'^{\mathrm{v}}$) and strain ($\boldsymbol{\varepsilon}'^{\mathrm{v}}$) tensors in Voigt notations as

$$\boldsymbol{\sigma}'^{\mathrm{v}} = \mathbf{T}\boldsymbol{\sigma}^{\mathrm{v}} \quad \text{and} \quad \boldsymbol{\varepsilon}'^{\mathrm{v}} = \mathbf{R}\mathbf{T}\mathbf{R}^{-1}\boldsymbol{\varepsilon}^{\mathrm{v}}.$$

Here $\mathbf{T}$ and $\mathbf{R}$ are the rotation and Reuter matrices, respectively, which can be expressed as

$$\mathbf{T} = \begin{bmatrix} P_{11}^2 & P_{21}^2 & 2P_{11}P_{21} \\ P_{12}^2 & P_{22}^2 & 2P_{12}P_{22} \\ P_{11}P_{12} & P_{21}P_{22} & P_{11}P_{22} + P_{12}P_{21} \end{bmatrix} \quad \text{and} \quad \mathbf{R} = \begin{bmatrix} 1 & 0 & 0 \\ 0 & 1 & 0 \\ 0 & 0 & 2 \end{bmatrix}.$$

In addition, the matrix $\mathbf{P} := \mathbf{Q}^{-1} = \mathbf{Q}^{\top}$ is the inverse rotation matrix. We then have

$$\mathbf{T} = \begin{bmatrix} \cos^2\overline{\varphi} & \sin^2\overline{\varphi} & -\sin(2\overline{\varphi}) \\ \sin^2\overline{\varphi} & \cos^2\overline{\varphi} & \sin(2\overline{\varphi}) \\ \sin(2\overline{\varphi})/2 & -\sin(2\overline{\varphi})/2 & \cos(2\overline{\varphi}) \end{bmatrix} \quad \text{and} \quad \mathbf{R}\mathbf{T}\mathbf{R}^{-1} = \begin{bmatrix} \cos^2\overline{\varphi} & \sin^2\overline{\varphi} & -\sin(2\overline{\varphi})/2 \\ \sin^2\overline{\varphi} & \cos^2\overline{\varphi} & \sin(2\overline{\varphi})/2 \\ \sin(2\overline{\varphi}) & -\sin(2\overline{\varphi}) & \cos(2\overline{\varphi}) \end{bmatrix},$$

which renders

$$\boldsymbol{\sigma}'^{\mathrm{v}} = \mathbf{D}'\boldsymbol{\varepsilon}'^{\mathrm{v}} \quad \Rightarrow \quad \mathbf{T}\boldsymbol{\sigma}^{\mathrm{v}} = \mathbf{D}'\mathbf{R}\mathbf{T}\mathbf{R}^{-1}\boldsymbol{\varepsilon}^{\mathrm{v}} \quad \Rightarrow \quad \boldsymbol{\sigma}^{\mathrm{v}} = \mathbf{T}^{-1}\mathbf{D}'\mathbf{R}\mathbf{T}\mathbf{R}^{-1}\boldsymbol{\varepsilon}^{\mathrm{v}}.$$

Here, $\mathbf{D}'$ is the rotated elasticity matrix to be determined. Considering $\boldsymbol{\sigma}^{\mathrm{v}} = \mathbf{D}\boldsymbol{\varepsilon}^{\mathrm{v}}$ with $\mathbf{D}$ representing the elasticity matrix before rotation, we derive the rotated elasticity matrix as

$$\mathbf{D}' = \mathbf{T}\mathbf{D}(\mathbf{R}\mathbf{T}\mathbf{R}^{-1})^{-1} = \mathbf{T}\mathbf{D}\mathbf{T}^{\top}$$

where we use the fact $(\mathbf{R}\mathbf{T}\mathbf{R}^{-1})^{-1} = \mathbf{T}^{\top}$.

Appendix E. Sensitivity analysis and verification

The topology optimization formulation proposed in Section 4.3 involves three groups of design variables — density, frequency, and transformation — with different filtering and projection operations. In addition, a neural network is also embedded in this formulation for computing the elasticity matrix. To furnish gradient information for solution updates in this complex design problem, in this section, we introduce the sensitivity analysis based on the adjoint method (Bendsoe and Sigmund, 2003) alongside automatic differentiation provided by FEniCSx (Baratta et al., 2023) and PyTorch (Ketkar et al., 2021) software. We also verify the sensitivity analysis through a comparison with the finite difference scheme.

E.1. Sensitivity analysis

To perform sensitivity analysis, we consider a general objective or constraint function

$$J(\overline{\boldsymbol{\rho}}; \overline{\boldsymbol{\xi}}_1, \overline{\boldsymbol{\xi}}_2, \dots, \overline{\boldsymbol{\xi}}_{M^{\text{freq}}}; \overline{\boldsymbol{\chi}}, \overline{\boldsymbol{\theta}}, \overline{\boldsymbol{\varphi}}),$$

where the bold Greek letters are the global vectors containing the projected design variables of all finite elements. We can write out the function's Lagrangian form as

$$\widehat{J}(\overline{\boldsymbol{\rho}}; \overline{\boldsymbol{\xi}}_1, \overline{\boldsymbol{\xi}}_2, \dots, \overline{\boldsymbol{\xi}}_{M^{\text{freq}}}; \overline{\boldsymbol{\chi}}, \overline{\boldsymbol{\theta}}, \overline{\boldsymbol{\varphi}}) = J + \mathbf{R} \cdot \boldsymbol{\lambda}$$

where $\mathbf{R}$ is the global residual vector, and $\boldsymbol{\lambda}$ is an adjoint vector to be determined and subjected to $\lambda_i = 0$ if DOF i is constrained in FEA.

Taking the derivative for the density vector ($\overline{\boldsymbol{\rho}}$) yields

$$\frac{\mathrm{d}\widehat{J}}{\mathrm{d}\overline{\boldsymbol{\rho}}} = \frac{\partial J}{\partial \overline{\boldsymbol{\rho}}} + \left(\frac{\partial \mathbf{U}}{\partial \overline{\boldsymbol{\rho}}}\right)^{\top} \frac{\partial J}{\partial \mathbf{U}} + \left[\left(\frac{\partial \mathbf{R}}{\partial \overline{\boldsymbol{\rho}}}\right)^{\top} + \left(\frac{\partial \mathbf{U}}{\partial \overline{\boldsymbol{\rho}}}\right)^{\top} \left(\frac{\partial \mathbf{R}}{\partial \mathbf{U}}\right)^{\top}\right] \boldsymbol{\lambda}.$$

Regrouping terms derives

$$\frac{\mathrm{d}\widehat{J}}{\mathrm{d}\overline{\boldsymbol{\rho}}} = \frac{\partial J}{\partial \overline{\boldsymbol{\rho}}} + \left(\frac{\partial \mathbf{R}}{\partial \overline{\boldsymbol{\rho}}}\right)^{\top} \boldsymbol{\lambda} + \left(\frac{\partial \mathbf{U}}{\partial \overline{\boldsymbol{\rho}}}\right)^{\top} \left[\frac{\partial J}{\partial \mathbf{U}} + \left(\frac{\partial \mathbf{R}}{\partial \mathbf{U}}\right)^{\top} \boldsymbol{\lambda}\right].$$

Eliminating the computationally expensive term, $(\partial \mathbf{U}/\partial \overline{\boldsymbol{\rho}})^{\top}$, gives the adjoint equation

$$\left(\frac{\partial \mathbf{R}}{\partial \mathbf{U}}\right)^{\top} \boldsymbol{\lambda} = -\frac{\partial J}{\partial \mathbf{U}} \quad \text{subjected to} \quad \lambda_i = 0 \text{ if DOF } i \text{ is constrained,} \tag{E.1}$$

where $\mathbf{U}$ is the global displacement vector. Finally, we obtain the sensitivity as

$$\frac{\mathrm{d}J}{\mathrm{d}\overline{\boldsymbol{\rho}}} = \frac{\mathrm{d}\widehat{J}}{\mathrm{d}\overline{\boldsymbol{\rho}}} = \frac{\partial J}{\partial \overline{\boldsymbol{\rho}}} + \left(\frac{\partial \mathbf{R}}{\partial \overline{\boldsymbol{\rho}}}\right)^{\top} \boldsymbol{\lambda} \tag{E.2}$$

with $\boldsymbol{\lambda}$ solved from the adjoint equation in (E.1). Similarly, the sensitivity analysis for the rotation vector can be computed as

$$\frac{\mathrm{d}J}{\mathrm{d}\overline{\boldsymbol{\varphi}}} = \frac{\partial J}{\partial \overline{\boldsymbol{\varphi}}} + \left(\frac{\partial \mathbf{R}}{\partial \overline{\boldsymbol{\varphi}}}\right)^{\top} \boldsymbol{\lambda}. \tag{E.3}$$

We now focus on the sensitivity analysis concerning the frequency vectors ($\overline{\boldsymbol{\xi}}_1, \overline{\boldsymbol{\xi}}_2, \dots, \overline{\boldsymbol{\xi}}_{M^{\text{freq}}}$) as well as relative scaling ($\overline{\boldsymbol{\chi}}$) and skew ($\overline{\boldsymbol{\theta}}$) vectors, which are indirectly related to the given function (J) through the components of the elasticity matrix predicted by a neural network. Following the previous procedure, we express the derivatives of the given function for the elasticity component vectors as

$$\frac{\mathrm{d}J}{\mathrm{d}\mathbf{c}_i} = \frac{\partial J}{\partial \mathbf{c}_i} + \left(\frac{\partial \mathbf{R}}{\partial \mathbf{c}_i}\right)^{\top} \boldsymbol{\lambda} \quad \text{for} \quad i = 1, 2, \dots, N^{\text{comp}},$$

where $\mathbf{c}_i$ is the global vector containing the ith independent component of the elasticity matrix for all finite elements, and N^{comp} is the number of independent components. We can then write out the sensitivities as

$$\frac{\mathrm{d}J}{\mathrm{d}\overline{\boldsymbol{\phi}}} = \sum_{i=1}^{N^{\text{comp}}} \left(\frac{\mathrm{d}\mathbf{c}_i}{\mathrm{d}\overline{\boldsymbol{\phi}}}\right)^{\top} \frac{\mathrm{d}J}{\mathrm{d}\mathbf{c}_i} \quad \text{for} \quad \overline{\boldsymbol{\phi}} \in \{\overline{\boldsymbol{\xi}}_1, \overline{\boldsymbol{\xi}}_2, \dots, \overline{\boldsymbol{\xi}}_{M^{\text{freq}}}, \overline{\boldsymbol{\chi}}, \overline{\boldsymbol{\theta}}\}. \tag{E.4}$$

Based on (E.1)–(E.4), we observe that, to evaluate the sensitivities, we only need to compute

$$\frac{\partial J}{\partial \overline{\boldsymbol{\mu}}} \quad \text{and} \quad \frac{\partial \mathbf{R}}{\partial \overline{\boldsymbol{\mu}}} \quad \text{for} \quad \overline{\boldsymbol{\mu}} \in \{\mathbf{U}, \overline{\boldsymbol{\rho}}, \overline{\boldsymbol{\varphi}}, \mathbf{c}_1, \mathbf{c}_2, \dots, \mathbf{c}_{N^{\text{comp}}}\} \tag{E.5}$$

and

$$\frac{\mathrm{d}\mathbf{c}_i}{\mathrm{d}\overline{\boldsymbol{\phi}}} \quad \text{for} \quad i = 1, 2, \dots, N^{\text{comp}} \text{ and } \overline{\boldsymbol{\phi}} \in \{\overline{\boldsymbol{\xi}}_1, \overline{\boldsymbol{\xi}}_2, \dots, \overline{\boldsymbol{\xi}}_{M^{\text{freq}}}, \overline{\boldsymbol{\chi}}, \overline{\boldsymbol{\theta}}\}. \tag{E.6}$$

To compute the derivatives in (E.5), we leverage the automatic differentiation in the FEniCSx package (Baratta et al., 2023). For the derivatives in (E.6), they are the gradients used in the backpropagation of a neural network, and therefore we can employ automatic differentiation provided by the PyTorch package (Ketkar et al., 2021). We also note that the sensitivities in (E.2)–(E.4) are with respect to the projected design vectors. To compute the sensitivities concerning the initial design vectors, we apply the chain rules and utilize the reverse operations of the linear filter (Bourdin, 2001), Heaviside projection (Bendsoe and Sigmund, 2003), and normalization projection (Jia et al., 2024b).

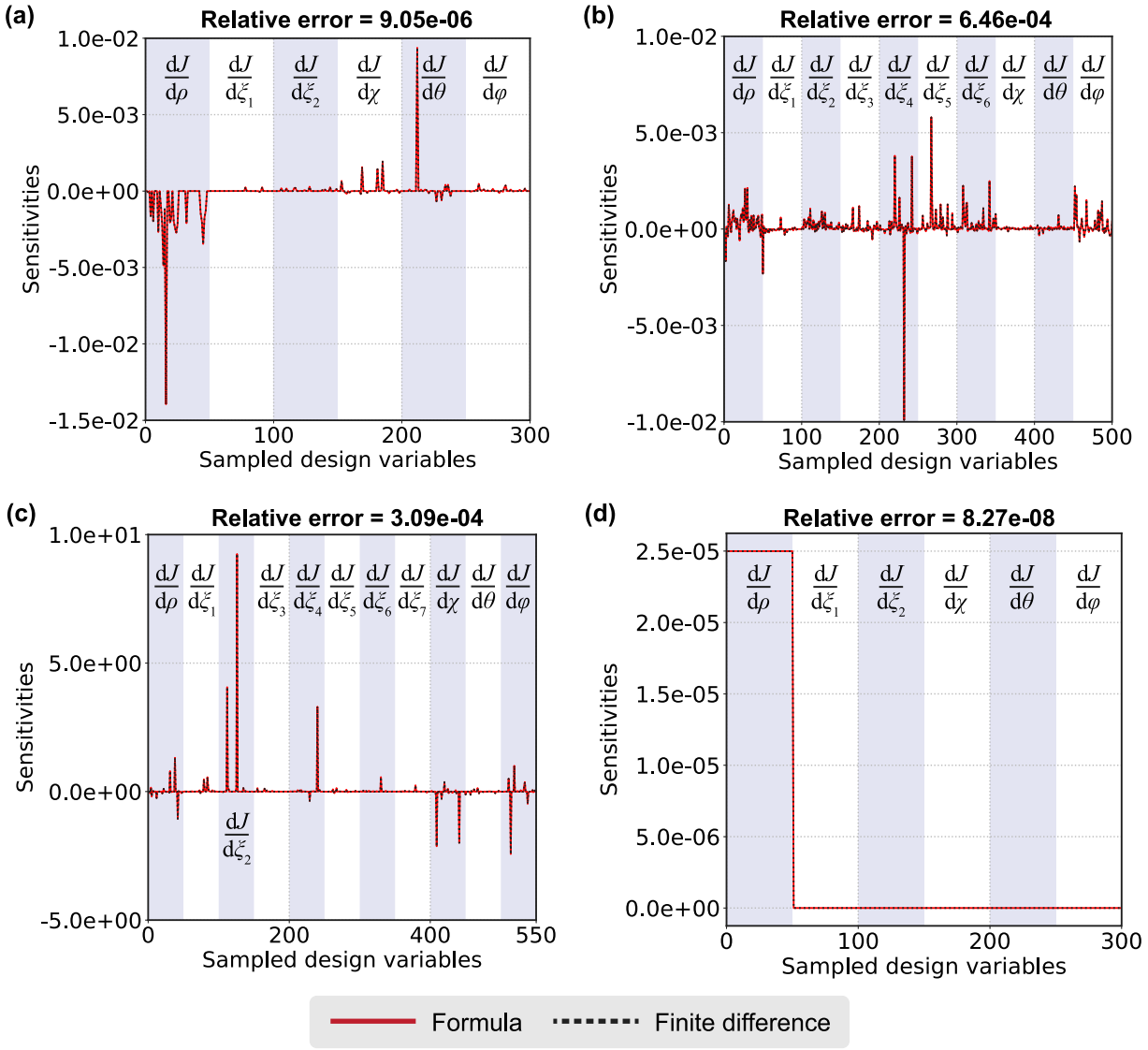

Fig. E.15. Comparison between the sensitivity values derived from the proposed formulae in (E.2)–(E.4) and the finite difference scheme for various objective and constraint functions. (a) Objective function (strain energy) for the transformed metastructure in Fig. 8(b). (b) Objective function (displacement fitting error) for metastructure 2 in Fig. 10(a). (c) Objective function (local stiffness) for the optimized metastructure in Fig. 13(a). (d) Constraint function (material volume fraction) for the transformed metastructure in Fig. 8(b).

E.2. Sensitivity verification

In this section, we verify the sensitivity expressions in (E.2)–(E.4) by comparing them with the forward finite difference scheme. The latter is expressed as

$$\frac{\mathrm{d}J}{\mathrm{d}\psi} \approx \frac{J(\psi+\varepsilon)-J(\psi)}{\varepsilon} \quad \text{for} \quad \psi \in \{\rho, \xi_1, \xi_2, \ldots, \xi_{M^{\mathrm{freq}}}, \chi, \theta, \varphi\}.$$

To perform this comparison, we use the stratified sampling strategy to randomly sample 50 finite elements for each design variable and examine the sensitivities for various objective and constraint functions used in Section 5. The comparison is shown in Fig. E.15, where we present the sensitivities for all design variables even if parts of them are not optimized. Based on the comparison, the sensitivity values derived from (E.2)–(E.4) closely align with the ones computed by the finite difference scheme as quantified by the small relative errors ranging from 3.09^{-4}–8.27^{-8}, indicating the accuracy of the sensitivity analysis in Appendix E.1.

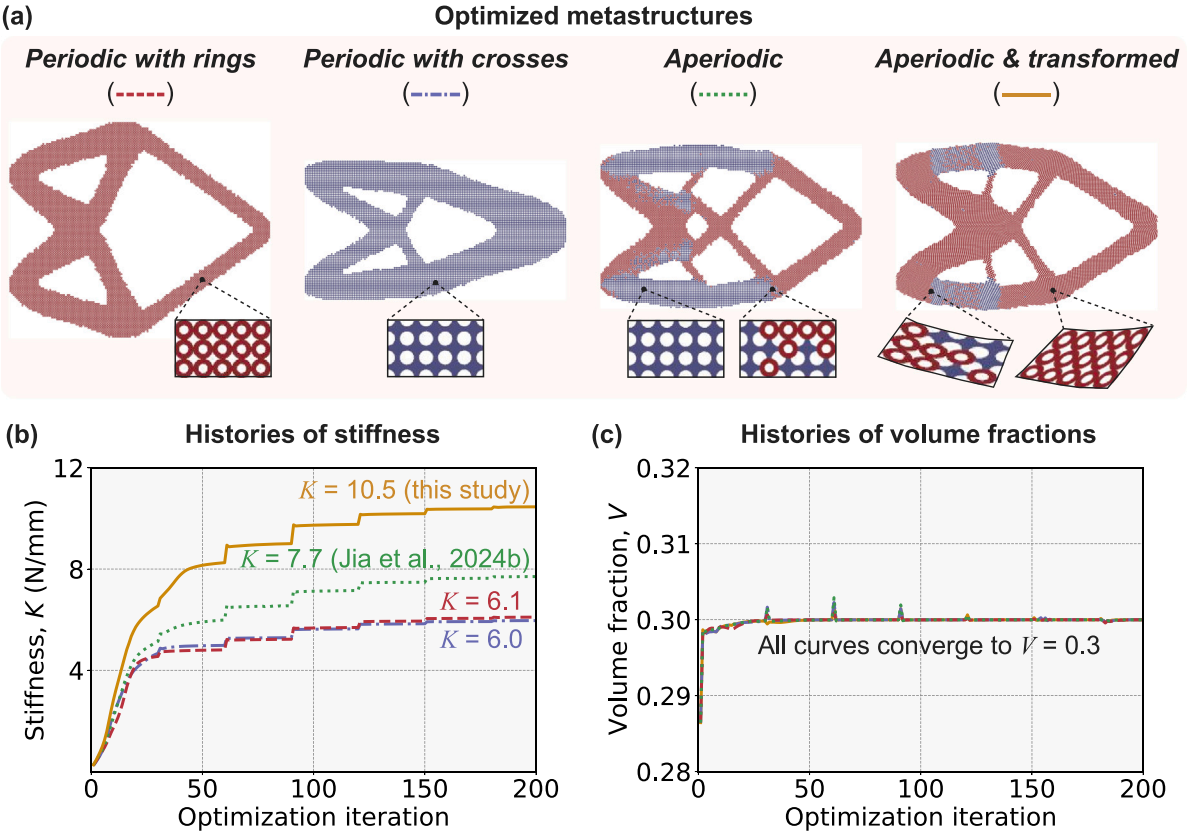

Fig. F.16. Comparison between periodic and aperiodic metastructures for stiffness maximization. (a) Optimized periodic and aperiodic metastructures. The lines in the parentheses serve as legends used in (b) and (c). (b) Optimization histories of structural stiffness (K). (c) Optimization histories of macroscale material volume fractions (V).

Appendix F. Comparison between periodic and aperiodic metastructures for stiffness maximization

In this section, we compare optimized periodic and aperiodic metastructures to illustrate the stiffness improvement achieved through aperiodicity and transformation. Fig. F.16(a) presents four metastructures with maximized stiffness. The first two metastructures are periodic, composed of `ring` and `cross` building blocks, respectively. The third metastructure (untransformed design in Fig. 8) introduces aperiodicity by allowing a mixed use of `ring` and `cross` building blocks. The last metastructure (transformed design in Fig. 8) incorporates both aperiodicity and microstructural transformation. All these metastructures are optimized under the same setup and the same volume fraction as described in Section 5.1.

To compare the periodic and aperiodic metastructures, we present the optimization histories of structural stiffness (K) in Fig. F.16(b). According to this figure, the stiffness of periodic metastructures with `ring` and `cross` building blocks converge to 6.1 and 6.0 N/mm^2, respectively. Allowing the mixed use of building blocks (the approach in Jia et al. (2024b)), the aperiodic design improves the stiffness to 7.7 N/mm^2, demonstrating increases of 26.2% and 28.3% compared to the two periodic designs, respectively. Furthermore, by enabling both aperiodicity and microstructural transformation (the method proposed in this study), the optimized metastructure elevates the structural stiffness to 10.5 N/mm^2, showing increases of 72.1% and 75.0% compared to the two periodic designs, respectively. This comparison highlights the performance gain enabled by introducing aperiodicity and microstructural transformation, and it is important to note again that all metastructures share the same material volume fraction (Fig. F.16(c)).

References

Baratta, I.A., Dean, J.P., Dokken, J.S., Habera, M., Hale, J.S., Richardson, C.N., Rognes, M.E., Scroggs, M.W., Sime, N., Wells, G.N., 2023. DOLFINx: The next generation FEniCS problem solving environment. Zenodo, http://dx.doi.org/10.5281/zenodo.10447666.

Barbero, E.J., 2023. Finite Element Analysis of Composite Materials Using Abaqus®. CRC Press.

Barthelat, F., Li, C.-M., Comi, C., Espinosa, H.D., 2006. Mechanical properties of nacre constituents and their impact on mechanical performance. J. Mater. Res. 21 (8), 1977–1986. http://dx.doi.org/10.1557/jmr.2006.0239.

Bendsøe, M.P., Kikuchi, N., 1988. Generating optimal topologies in structural design using a homogenization method. Comput. Methods Appl. Mech. Engrg. 71 (2), 197–224. http://dx.doi.org/10.1016/0045-7825(88)90086-2.

Bendsoe, M.P., Sigmund, O., 2003. Topology Optimization: Theory, Methods, and Applications. Springer Science & Business Media.
Bommes, D., Zimmer, H., Kobbelt, L., 2009. Mixed-integer quadrangulation. ACM Trans. Graph. 28 (3), 1–10. http://dx.doi.org/10.1145/1531326.1531383.
Bourdin, B., 2001. Filters in topology optimization. Internat. J. Numer. Methods Engrg. 50 (9), 2143–2158. http://dx.doi.org/10.1002/nme.116.
Bradski, G., 2000. The opencv library. Dr. Dobb's J.: Softw. Tools Profess. Programm. 25 (11), 120–123.
Cai, P., Wang, C., Gao, H., Chen, X., 2021. Mechanomaterials: A rational deployment of forces and geometries in programming functional materials. Adv. Mater. 33 (46), 2007977. http://dx.doi.org/10.1002/adma.202007977.
Chen, Y., Hu, G., Huang, G., 2017. A hybrid elastic metamaterial with negative mass density and tunable bending stiffness. J. Mech. Phys. Solids 105, 179–198. http://dx.doi.org/10.1016/j.jmps.2017.05.009.
Chen, J., Wu, H., Zhou, J., Li, Z., Duan, K., Xu, R., Jiang, T., Jiang, H., Fan, R., Ballarini, R., Lu, Y., 2024. Heterostructured mechanical metamaterials inspired by the shell of Strombus Gigas. J. Mech. Phys. Solids 188, 105658. http://dx.doi.org/10.1016/j.jmps.2024.105658.
Clausen, A., Wang, F., Jensen, J.S., Sigmund, O., Lewis, J.A., 2015. Topology optimized architectures with programmable Poisson's ratio over large deformations. Adv. Mater. 27 (37), 5523–5527. http://dx.doi.org/10.1002/adma.201502485.
Deng, B., Wang, S., Hartquist, C., Zhao, X., 2023. Nonlocal intrinsic fracture energy of polymerlike networks. Phys. Rev. Lett. 131 (22), 228102. http://dx.doi.org/10.1103/PhysRevLett.131.228102.
Geuzaine, C., Remacle, J.-F., 2009. Gmsh: A 3-D finite element mesh generator with built-in pre-and post-processing facilities. Int. J. Num Methods Eng. 79 (11), 1309–1331.
Groen, J.P., Thomsen, C.R., Sigmund, O., 2021. Multi-scale topology optimization for stiffness and de-homogenization using implicit geometry modeling. Struct. Multidiscip. Optim. 63 (6), 2919–2934. http://dx.doi.org/10.1007/s00158-021-02874-7.
Hosoya, T., Kawamoto, H., Saka, S., 2007. Cellulose–hemicellulose and cellulose–lignin interactions in wood pyrolysis at gasification temperature. J. Anal. Appl. Pyrol. 80 (1), 118–125. http://dx.doi.org/10.1016/j.jaap.2007.01.006.
Hughes, T.J.R., 2012. The Finite Element Method: Linear Static and Dynamic Finite Element Analysis. Courier Corporation.
Jensen, P.D.L., Olsen, T.F., Bærentzen, J.A., Aage, N., Sigmund, O., 2024. Efficient inverse-designed structural infill for complex engineering structures. Thin-Walled Struct. 195, 111427. http://dx.doi.org/10.1016/j.tws.2023.111427.
Jia, Y., Liu, K., Zhang, X.S., 2024a. Modulate stress distribution with bio-inspired irregular architected materials towards optimal tissue support. Nature Commun. 15 (1), 4072. http://dx.doi.org/10.1038/s41467-024-47831-2.
Jia, Y., Liu, K., Zhang, X.S., 2024b. Topology optimization of irregular multiscale structures with tunable responses using a virtual growth rule. Comput. Methods Appl. Mech. Engrg. 425, 116864. http://dx.doi.org/10.1016/j.cma.2024.116864.
Jia, Y., Lopez-Pamies, O., Zhang, X.S., 2023. Controlling the fracture response of structures via topology optimization: From delaying fracture nucleation to maximizing toughness. J. Mech. Phys. Solids 173, 105227. http://dx.doi.org/10.1016/j.jmps.2023.105227.
Jia, Y., Wang, C., Zhang, X.S., 2024c. FEniTop: A simple FEniCSx implementation for 2D and 3D topology optimization supporting parallel computing. Struct. Multidiscip. Optim. Accepted.
Ketkar, N., Moolayil, J., Ketkar, N., Moolayil, J., 2021. Introduction to pytorch. In: Deep Learning with Python: Learn Best Practices of Deep Learning Models with Pytorch. Springer, pp. 27–91.
Kingma, D.P., Ba, J., 2017. Adam: A method for stochastic optimization. http://dx.doi.org/10.48550/arXiv.1412.6980.
Kumar, S., Tan, S., Zheng, L., Kochmann, D.M., 2020. Inverse-designed spinodoid metamaterials. npj Comput. Mater. 6 (1), 1–10. http://dx.doi.org/10.1038/s41524-020-0341-6.
Li, W., Jia, Y., Wang, F., Sigmund, O., Zhang, X.S., 2023. Programming and physical realization of extreme three-dimensional responses of metastructures under large deformations. Internat. J. Engrg. Sci. 191, 103881. http://dx.doi.org/10.1016/j.ijengsci.2023.103881.
Li, S., Zhu, Y., Guo, X., 2022. Optimisation of spatially varying orthotropic porous structures based on conformal mapping. Comput. Methods Appl. Mech. Engrg. 391, 114589. http://dx.doi.org/10.1016/j.cma.2022.114589.
Liu, K., Sun, R., Daraio, C., 2022. Growth rules for irregular architected materials with programmable properties. Science 377 (6609), 975–981. http://dx.doi.org/10.1126/science.abn1459.
Ma, C., Xue, D., Li, S., Zhou, Z., Zhu, Y., Guo, X., 2021. Stiffness minimisation of graded microstructural configurations using asymptotic analysis and machine learning. arXiv:2110.06458.
Magrini, T., Fox, C., Wihardja, A., Kolli, A., Daraio, C., 2024. Control of mechanical and fracture properties in two-phase materials reinforced by continuous, irregular networks. Adv. Mater. 36 (6), 2305198. http://dx.doi.org/10.1002/adma.202305198.
Mirzaali, M.J., Pahlavani, H., Zadpoor, A.A., 2019. Auxeticity and stiffness of random networks: Lessons for the rational design of 3D printed mechanical metamaterials. Appl. Phys. Lett. 115 (2), 021901. http://dx.doi.org/10.1063/1.5096590.
Ni, B., Gao, H., 2019. Engineer energy dissipation in 3D graphene nanolattice via reversible snap-through instability. J. Appl. Mech. 87 (031012), http://dx.doi.org/10.1115/1.4045544.
Ou, H., Hu, L., Wang, Y., Liu, C., 2024. High-efficient and reusable impact mitigation metamaterial based on compression-torsion coupling mechanism. J. Mech. Phys. Solids 186, 105594. http://dx.doi.org/10.1016/j.jmps.2024.105594.
Portela, C.M., Vidyasagar, A., Krödel, S., Weissenbach, T., Yee, D.W., Greer, J.R., Kochmann, D.M., 2020. Extreme mechanical resilience of self-assembled nanolabyrinthine materials. Proc. Natl. Acad. Sci. 117 (11), 5686–5693. http://dx.doi.org/10.1073/pnas.1916817117.
Reid, D.R., Pashine, N., Wozniak, J.M., Jaeger, H.M., Liu, A.J., Nagel, S.R., de Pablo, J.J., 2018. Auxetic metamaterials from disordered networks. Proc. Natl. Acad. Sci. 115 (7), E1384–E1390. http://dx.doi.org/10.1073/pnas.1717442115.
Rhee, H., Horstemeyer, M.F., Hwang, Y., Lim, H., El Kadiri, H., Trim, W., 2009. A study on the structure and mechanical behavior of the terrapene Carolina carapace: A pathway to design bio-inspired synthetic composites. Mater. Sci. Eng.: C 29 (8), 2333–2339. http://dx.doi.org/10.1016/j.msec.2009.06.002.
Rho, J.-Y., Kuhn-Spearing, L., Zioupos, P., 1998. Mechanical properties and the hierarchical structure of bone. Med. Eng. Phys. 20 (2), 92–102. http://dx.doi.org/10.1016/S1350-4533(98)00007-1.
Senhora, F.V., Sanders, E.D., Paulino, G.H., 2022. Optimally-tailored spinodal architected materials for multiscale design and manufacturing. Adv. Mater. 34 (26), 2109304. http://dx.doi.org/10.1002/adma.202109304.
Sharma, D., Hiremath, S.S., 2022. In-plane and out-plane flexural properties of the bird feather-inspired panels: Experimental, digital image correlation, and finite element study. Aerosp. Sci. Technol. 127, 107731. http://dx.doi.org/10.1016/j.ast.2022.107731.
Stutz, F.C., Groen, J.P., Sigmund, O., Bærentzen, J.A., 2020. Singularity aware de-homogenization for high-resolution topology optimized structures. Struct. Multidiscip. Optim. 62 (5), 2279–2295. http://dx.doi.org/10.1007/s00158-020-02681-6.
Svanberg, K., 1987. The method of moving asymptotes—a new method for structural optimization. Internat. J. Numer. Methods Engrg. 24 (2), 359–373. http://dx.doi.org/10.1002/nme.1620240207.
Vigliotti, A., Pasini, D., 2012. Stiffness and strength of tridimensional periodic lattices. Comput. Methods Appl. Mech. Engrg. 229–232, 27–43. http://dx.doi.org/10.1016/j.cma.2012.03.018.
Visvalingam, M., Whyatt, J.D., 1990. The Douglas-Peucker Algorithm for line simplification: re-evaluation through visualization. Comput. Graph. Forum 9 (3), 213–225. http://dx.doi.org/10.1111/j.1467-8659.1990.tb00398.x.
Wang, L., Boddapati, J., Liu, K., Zhu, P., Daraio, C., Chen, W., 2022a. Mechanical cloak via data-driven aperiodic metamaterial design. Proc. Natl. Acad. Sci. 119 (13), e2122185119. http://dx.doi.org/10.1073/pnas.2122185119.

Wang, L., Liu, Z., Da, D., Chan, Y.-C., Chen, W., Zhu, P., 2022b. Generalized de-homogenization via sawtooth-function-based mapping and its demonstration on data-driven frequency response optimization. Comput. Methods Appl. Mech. Engrg. 395, 114967. http://dx.doi.org/10.1016/j.cma.2022.114967.

Wang, C., Zhao, Z., Zhou, M., Sigmund, O., Zhang, X.S., 2021. A comprehensive review of educational articles on structural and multidisciplinary optimization. Struct.Multidiscip. Optim. 64, 2827–2880. http://dx.doi.org/10.1007/s00158-021-03050-7.

Wu, J., Sigmund, O., Groen, J.P., 2021. Topology optimization of multi-scale structures: A review. Struct. Multidiscip. Optim. 63 (3), 1455–1480. http://dx.doi.org/10.1007/s00158-021-02881-8.

Zhang, H., Guo, X., Wu, J., Fang, D., Zhang, Y., 2018a. Soft mechanical metamaterials with unusual swelling behavior and tunable stress-strain curves. Sci. Adv. 4 (6), eaar8535. http://dx.doi.org/10.1126/sciadv.aar8535.

Zhang, X., Yao, J., Liu, B., Yan, J., Lu, L., Li, Y., Gao, H., Li, X., 2018b. Three-dimensional high-entropy alloy–polymer composite nanolattices that overcome the strength–recoverability trade-off. Nano Lett. 18 (7), 4247–4256. http://dx.doi.org/10.1021/acs.nanolett.8b01241.

Zheng, L., Kumar, S., Kochmann, D.M., 2021. Data-driven topology optimization of spinodoid metamaterials with seamlessly tunable anisotropy. Comput. Methods Appl. Mech. Engrg. 383, 113894. http://dx.doi.org/10.1016/j.cma.2021.113894.

Zhu, Y., Li, S., Du, Z., Liu, C., Guo, X., Zhang, W., 2019. A novel asymptotic-analysis-based homogenisation approach towards fast design of infill graded microstructures. J. Mech. Phys. Solids 124, 612–633. http://dx.doi.org/10.1016/j.jmps.2018.11.008.